



# Calculation of predictions for non-identical particle correlations in heavy ions collisions at LHC energies from hydrodynamics-inspired models

MASTER OF SCIENCE THESIS

Author:  
**Mateusz Wojciech Gałażyn**

Supervisor:  
**Prof. Adam Kisiel**

Warsaw, 30th November 2014



# Wyznaczenie przewidywań teoretycznych dla korelacji cząstek nieidentycznych w zderzeniach ciężkich jonów przy energiach LHC w modelach opartych na hydrodynamice

PRACA MAGISTERSKA

Autor:  
**Mateusz Wojciech Gałażyn**

Promotor:  
**dr hab. inż. Adam Kisiel, prof. PW**

Warszawa, 30 listopada 2014

## 1 Abstract

2 This thesis presents results of two-particle momentum correlations analysis  
3 for different kinds of particles produced in heavy ion collisions. The studies  
4 were carried for the data from lead-lead collisions at the centre of mass  
5 energy  $\sqrt{s_{NN}} = 2.76$  TeV simulated in the THERMINATOR model using the  
6 (3+1)-dimensional hydrodynamic model with viscosity. Analysis was performed  
7 for the three particle kinds: pions, kaons and protons for the collisions in eight  
8 different centrality ranges.

9 The THERMINATOR model allows to perform statistical hadronization of  
10 stable particles and unstable resonances from a given hypersurface which is  
11 followed by the resonance propagation and decay phase. The four-dimensional  
12 hypersurface is coming from the calculations performed on a basis of relativistic  
13 hydrodynamic framework with the viscosity corrections.

14 One can investigate space-time characteristics of the particle-emitting source  
15 through two-particle interferometry using experimental observables. The  
16 experimental-like analysis of the data coming from a model calculations yields  
17 a possibility to test the hydrodynamic description of a quark-gluon plasma.  
18 This thesis concentrates on the verification of the prediction of appearance of  
19 femtoscopic radii scaling with the transverse mass.

20 The three dimensional correlation functions were calculated using spherical  
21 harmonics decomposition. One can use this approach to perform calculations  
22 with lower statistics and the visualization of results is much easier. The calcu-  
23 lated correlation functions show expected increase of a correlation for pions and  
24 kaons at the low relative momenta of a pair. For the protons at the same mo-  
25 mentum region, the decrease occurs. The transverse pair momentum and cen-  
26 trality dependence on a correlation function is observed. In order to perform the  
27 quantitative analysis of this influence, the fitting of theoretical formula for cor-  
28 relation function was performed. The femtoscopic radii calculated in the LCMS  
29 and PRF are falling with the transverse mass  $m_T$ . To test the scaling predicted  
30 from the hydrodynamics, the power law was fitted  $\alpha m_T^{-\beta}$ . The radii calculated  
31 for pions, kaons and protons in the LCMS are following the common scaling. In  
32 case of the PRF no such scaling is observed. To recover the scaling in the PRF, the  
33 approximate factor is proposed:  $\sqrt{(\sqrt{\gamma_T} + 2)/3}$ . The radii in the PRF divided by  
34 the proposed scaling factor are falling on the common curve, therefore the scaling  
35 can be recovered using the proposed scaling factor. The experimental analysis is  
36 usually performed in the PRF (requires less statistics), hence the method of scal-  
37 ing recovery enables easier testing of the hydrodynamic predictions, which are  
38 not visible in the PRF.

## Streszczenie

40 W tej pracy zaprezentowane są wyniki analizy dwucząstkowych korelacji pę-  
41 dowych dla trzech różnych typów cząstek produkowanych w zderzeniach cięż-  
42 kich jonów. Obliczenia zostały wykonane dla danych ze zderzeń ołów-ołów przy  
43 energii w centrum masy  $\sqrt{s_{NN}} = 2.76$  TeV wygenerowanych za pomocą mo-  
44 delu THERMINATOR przy użyciu (3+1)-wymiarowego modelu hydrodynamicz-  
45 nego uwzględniającego lepkość ośrodka. Analiza została wykonana dla trzech  
46 rodzajów cząstek: pionów, kaonów i protonów dla dziewięciu różnych przedzia-  
47 łów centralności.

48 Model THERMINATOR pozwala na wykonanie statystycznej hadronizacji  
49 stabilnych cząstek jak i również niestabilnych rezonansów z danej  
50 hiperpowierzchni wymrażania oraz uwzględnienie propagacji i rozpadów  
51 tych rezonansów. Czterowymiarowa hiperpowierzchnia pochodzi z  
52 obliczeń przeprowadzonych na podstawie hydrodynamiki relatywistycznej z  
53 uwzględnieniem poprawek pochodzących od lepkości.

54 Interferometria dwucząstkowa pozwala na zbadanie charakterystyk  
55 czasowo-przestrzennych źródła cząstek. Poprzez analizę danych pochodzących  
56 z obliczeń modelowych można dokonać sprawdzenia zakresu stosownalności  
57 hydrodynamiki do opisu właściwości plazmy kwarkowo-gluonowej. Ta praca  
58 koncentruje się na weryfikacji skalowania promieni femtoskopowych z masą  
59 poprzeczną przewidywanego przez hydrodynamikę.

60 Trójwymiarowe funkcje korelacyjne zostały obliczone za pomocą rozkładu w  
61 szeregu harmonik sferycznych. To podejście wymaga mniejszej statystyki i po-  
62 zwala na łatwiejszą wizualizację wyników. Obliczone funkcje korelacyjne wy-  
63 kazują oczekiwany wzrost korelacji dla niskich różnic pędów dla par pionów i  
64 kaonów. Dla par protonów w tym samym zakresie pędów widoczny jest spa-  
65 dek korelacji. Widoczny jest wpływ pędu poprzecznego pary oraz centralności  
66 na funkcję korelacyjną. W celu wykonania analizy ilościowej tego wpływu, zo-  
67 stało wykonane dopasowanie formuły analitycznej do obliczonych funkcji kore-  
68 lacyjnych. Otrzymane w ten sposób promienie femtoskopowe w LCMS i PRF  
69 wykazują spadek wraz z wzrostem masy poprzecznej  $m_T$ . W celu sprawdzenie  
70 skalowania przewidywanego przez hydrodynamikę została dopasowana zależ-  
71 ność potęgowa:  $\alpha m_T^{-\beta}$ . Promienie obliczone dla pionów, kaonów i protonów  
72 zachowują wzajemne skalowanie w LCMS. W przypadku PRF skalowanie nie  
73 jest widoczne. Aby odzyskać skalowanie w PRF, został zaproponowany przy-  
74 bliżony współczynnik:  $\sqrt{(\sqrt{\gamma_T} + 2)/3}$ . Promienie w PRF po podzieleniu przez

<sup>75</sup> współczynnik skalowania, są opisywalne przez podaną zależność potęgową, za-  
<sup>76</sup> tem umożliwia on odzyskanie skalowania. Analiza eksperimentalna jest zazwy-  
<sup>77</sup> czaj wykonywana w PRF (wymaga mniejszej statystyki), zatem ta metoda po-  
<sup>78</sup> zwala na łatwiejszą weryfikację przewidywań hydrodynamiki które są widoczne  
<sup>79</sup> w LCMS, a nie są w PRF.

# <sup>80</sup> Contents

<sup>81</sup>	<b>Introduction</b>	<b>1</b>
<sup>82</sup>	<b>1 Theory of heavy ion collisions</b>	<b>3</b>
<sup>83</sup>	1.1 The Standard Model . . . . .	3
<sup>84</sup>	1.2 Quantum Chromodynamics . . . . .	4
<sup>85</sup>	1.2.1 Quarks and gluons . . . . .	4
<sup>86</sup>	1.2.2 Quantum Chromodynamics potential . . . . .	5
<sup>87</sup>	1.2.3 The quark-gluon plasma . . . . .	7
<sup>88</sup>	1.3 Relativistic heavy ion collisions . . . . .	9
<sup>89</sup>	1.3.1 Stages of heavy ion collision . . . . .	9
<sup>90</sup>	1.3.2 QGP signatures . . . . .	11
<sup>91</sup>	<b>2 Therminator model</b>	<b>19</b>
<sup>92</sup>	2.1 (3+1)-dimensional viscous hydrodynamics . . . . .	19
<sup>93</sup>	2.2 Statistical hadronization . . . . .	20
<sup>94</sup>	2.2.1 Cooper-Frye formalism . . . . .	21
<sup>95</sup>	2.3 Events generation procedure . . . . .	22
<sup>96</sup>	<b>3 Particle interferometry</b>	<b>25</b>
<sup>97</sup>	3.1 HBT interferometry . . . . .	25
<sup>98</sup>	3.2 Theoretical approach . . . . .	25
<sup>99</sup>	3.2.1 Conventions used . . . . .	26
<sup>100</sup>	3.2.2 Two particle wave function . . . . .	27
<sup>101</sup>	3.2.3 Source emission function . . . . .	28
<sup>102</sup>	3.2.4 Analytical form of a correlation function . . . . .	30
<sup>103</sup>	3.2.5 Spherical harmonics decomposition of a correlation function	31
<sup>104</sup>	3.3 Experimental approach . . . . .	32
<sup>105</sup>	3.4 Scaling of femtoscopic radii . . . . .	33
<sup>106</sup>	3.4.1 Scaling in LCMS . . . . .	34
<sup>107</sup>	3.4.2 Scaling in PRF . . . . .	35
<sup>108</sup>	<b>4 Results</b>	<b>36</b>
<sup>109</sup>	4.1 Identical particles correlations . . . . .	36
<sup>110</sup>	4.1.1 Spherical harmonics components . . . . .	36

111	4.1.2	Centrality dependence of a correlation function . . . . .	40
112	4.1.3	$k_T$ dependence of a correlation function . . . . .	41
113	4.2	Results of the fitting procedure . . . . .	42
114	4.2.1	The three-dimensional femtoscopic radii scaling . . . . .	42
115	4.2.2	Scaling of one-dimensional radii . . . . .	46
116	4.3	Discussion of the results . . . . .	47
117	<b>Conclusions</b>		<b>48</b>
118	<b>A</b>	<b>Scripts for events generation</b>	<b>50</b>
119	<b>B</b>	<b>Macros for fitting</b>	<b>52</b>
120	<b>C</b>	<b>Plotting scripts</b>	<b>53</b>

# <sup>121</sup> Introduction

<sup>122</sup> Many people were trying to discover what was in the beginning of the uni-  
<sup>123</sup> verse which we observe today. Through the years, more or less successful theo-  
<sup>124</sup> ries were appearing and trying to describe its origin and behaviour. Among them  
<sup>125</sup> is one model, which provides a comprehensive explanation for a broad range  
<sup>126</sup> of phenomena, including the cosmic microwave background, abundance of the  
<sup>127</sup> light elements and Hubble's law. This model is called The Big Bang theory and  
<sup>128</sup> has born in 1927 on the basis of principles proposed by the Belgian priest and  
<sup>129</sup> scientist Georges Lemaître. Using this model and known laws of physics one can  
<sup>130</sup> calculate the characteristics of the universe in detail back in time to the extreme  
<sup>131</sup> densities and temperatures. However, at some point these calculations fail. The  
<sup>132</sup> extrapolation of the expansion of universe backwards in time using general re-  
<sup>133</sup> lativity yields an infinite density and temperature at a finite time in the past. This  
<sup>134</sup> appearance of singularity is a signal of the breakdown of general relativity. The  
<sup>135</sup> range of this extrapolation towards singularity is debated - certainly we can go no  
<sup>136</sup> closer than the end of *Planck epoch* i.e.  $10^{-43}$  s. At this very first era the temperat-  
<sup>137</sup> ure of the universe was so high, that the four fundamental forces - electromagnet-  
<sup>138</sup> ism, gravitation, weak nuclear interaction and strong nuclear interaction - were  
<sup>139</sup> one fundamental force. Between  $10^{-43}$  s and  $10^{-36}$  s of a lifetime of the universe,  
<sup>140</sup> there is a *grand unification epoch*, at which forces are starting to separate from each  
<sup>141</sup> other. The *electroweak epoch* lasted from  $10^{-36}$  s to  $10^{-12}$  s, when the strong force  
<sup>142</sup> separated from the electroweak force. After the electroweak epoch, there was  
<sup>143</sup> the *quark epoch* in which the universe was a dense "soup" of quarks. During this  
<sup>144</sup> stage the fundamental forces of gravitation, electromagnetism, strong and weak  
<sup>145</sup> interactions had taken their present forms. The temperature at this moment was  
<sup>146</sup> still too high to allow quarks to bind together and form hadrons. At the end of  
<sup>147</sup> quark era, there was a big freeze-out - when the average energy of particle inter-  
<sup>148</sup> actions had fallen below the binding energy of hadrons. This era in which quarks  
<sup>149</sup> became confined into hadrons is known as the hadron epoch. At this moment the  
<sup>150</sup> matter had started forming nuclei and atoms, which we observe today.

<sup>151</sup> Here arises the question: how can we study the very beginning of the  
<sup>152</sup> universe? To do this, one should create in a laboratory a system with such a  
<sup>153</sup> large density and high temperature to recreate those conditions. Today, this is  
<sup>154</sup> achievable through sophisticated machines, which are particle accelerators. In  
<sup>155</sup> the particle accelerators, like the Large Hadron Collider at CERN, Geneva or

156 Relativistic Heavy Ion Collider at Brookhaven National Laboratory in Upton,  
157 New York, the heavy ions after being accelerated to near the speed of light are  
158 collided in order to generate extremely dense and hot phase of matter and  
159 recreate the quark-gluon plasma. The plasma is believed to behave like an  
160 almost ideal fluid and to become a medium, that can be described by the laws of  
161 relativistic hydrodynamics.

162 This thesis is providing predictions for collective behaviour of the quark-  
163 gluon plasma coming from the hydrodynamic equations. Experimental-like  
164 analysis was performed for the high energy Pb-Pb collisions generated with  
165 THERMINATOR model.

166 The 1st chapter is an introduction to the theory of heavy ion collisions. It  
167 contains the brief description of the Standard Model and Quantum Chromody-  
168 namics. The quark-gluon plasma and its signatures are also characterized.

169 In the 2nd chapter there is a description of the relativistic hydrodynamic  
170 framework and the THERMINATOR model used to perform the simulations of col-  
171 lisions.

172 The 3rd chapter covers the particle interferometry method used in this work.  
173 The algorithm of building experimental correlation functions and effects coming  
174 from the hydrodynamics in the experimental results for particle interferometry  
175 are also presented.

176 In the 4th chapter there is a detailed analysis of the results for two-particle  
177 femtoscopy for different pairs of particles. The quantitative analysis of calcu-  
178 lated femtoscopic radii as well as the appearance of transverse mass scaling is  
179 discussed.

# 180 Chapter 1

## 181 Theory of heavy ion collisions

### 182 1.1 The Standard Model

183 In the 1970s, a new theory of fundamental particles and their interaction  
184 emerged. It was a new concept, which combines the electromagnetic, weak and  
185 strong nuclear interactions between known particles. This theory is called *The  
186 Standard Model*. There are seventeen named particles in the standard model, or-  
187 ganized into the chart shown below (Fig. 1.1). Fundamental particles are divided  
into two families: *fermions* and *bosons*.

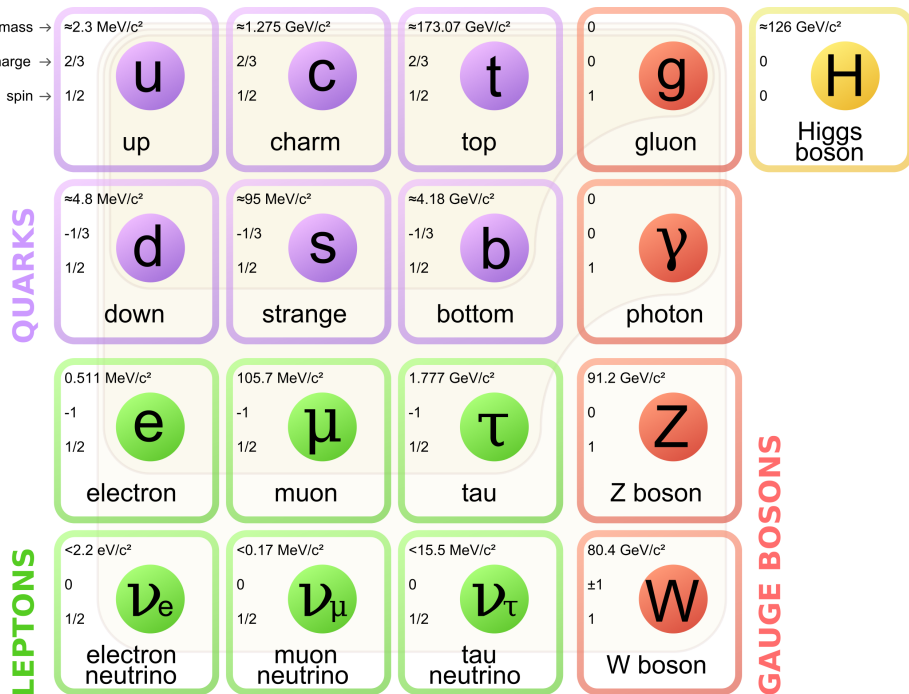


Figure 1.1: The Standard Model of elementary particles [1].

188 Fermions are the building blocks of matter. They are divided into two groups.  
 189 Six of them, which must bind together are called *quarks*. Quarks are known to  
 190 bind into doublets (*mesons*), triplets (*baryons*) and recently confirmed four-quark  
 191 states.<sup>1</sup> Two of baryons, with the longest lifetimes, are forming a nucleus: a pro-  
 192 ton and a neutron. A proton is build from two up quarks and one down, and  
 193 neutron consists of two down quarks and one up. A proton is found to be a stable  
 194 particle (at least it has a lifetime larger than  $10^{35}$  years) and a free neutron has a  
 195 mean lifetime about  $8.8 \times 10^2$  s. Fermions, that can exist independently are called  
 196 *leptons*. Neutrinos are a subgroup of leptons, which are only influenced by weak  
 197 interaction. Fermions can be divided into three generations (three columns in  
 198 the Figure 1.1). Generation I particles can combine into hadrons with the longest  
 199 life spans. Generation II and III consists of unstable particles which also form  
 200 unstable hadrons.

201 Bosons are force carriers. There are four fundamental forces: weak - respons-  
 202ible for radioactive decay, strong - coupling quarks into hadrons, electromagnetic  
 203 - between charged particles and gravity - the weakest, which causes the attraction  
 204 between particles with mass. The Standard Model describes the first three. The  
 205 weak force is mediated by  $W^\pm$  and  $Z^0$  bosons, electromagnetic force is carried by  
 206 photons  $\gamma$  and the carriers of a strong interaction are gluons  $g$ . The fifth boson is  
 207 a Higgs boson which is responsible for giving other particles mass.

## 208 1.2 Quantum Chromodynamics

### 209 1.2.1 Quarks and gluons

210 Quarks interact with each other through the strong interaction. The medi-  
 211 ator of this force is a *gluon* - a massless and electrical chargeless particle. In the  
 212 quantum chromodynamics (QCD) - theory describing strong interaction - there  
 213 are six types of "charges" (like electrical charges in the electrodynamics) called  
 214 *colours*. The colours were introduced because some of the observed particles, like  
 215  $\Delta^-$ ,  $\Delta^{++}$  and  $\Omega^-$  appeared to consist of three quarks with the same flavour (*ddd*,  
 216 *uuu* and *sss* respectively), which was in conflict with the Pauli principle. One  
 217 quark can carry one of the three colours (usually called *red*, *green* and *blue*) and anti-  
 218 quark one of the three anti-colours respectively. Only colour-neutral (or white)  
 219 particles could exist. Mesons are assumed to be a colour-anticolour pair, while  
 220 baryons are *red-green-blue* triplets. Gluons also are colour-charged and there are  
 221 8 types of gluons. Therefore they can interact with themselves [3].

---

<sup>1</sup>The LHCb experiment at CERN in Geneva confirmed recently the existence of  $Z(4430)$  - a particle consisting of four quarks [2].

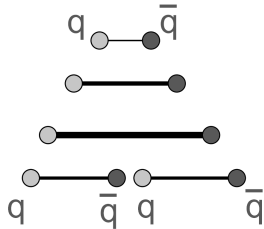
### 222 1.2.2 Quantum Chromodynamics potential

223 As a result of the fact that gluons are massless, one can expect, that the static  
 224 potential in QCD will have the form like similar one in electrodynamics e.g.  
 225  $\sim 1/r$  (by analogy to photons). In reality the QCD potential is assumed to have  
 226 the form of [3]

$$227 V_s = -\frac{4}{3} \frac{\alpha_s}{r} + kr, \quad (1.1)$$

227 where the  $\alpha_s$  is a coupling constant of the strong force and the  $kr$  part is related  
 228 with *confinement*. In comparison to the electromagnetic force, a value of the strong  
 229 coupling constant is  $\alpha_s \approx 1$  and the electromagnetic one is  $\alpha = 1/137$ .

230 The fact that quarks does not exist separately and are always bound, is called  
 231 confinement. As two quarks are pulled apart, the linear part  $kr$  in the Eq. 1.1  
 232 becomes dominant and the potential becomes proportional to the distance. This  
 233 situation resembles stretching of a string. At some point, when the string is so  
 234 large it is energetically favourable to create a quark-antiquark pair. At this  
 235 moment such pair (or pairs) is formed, the string breaks and the confinement is  
 preserved (Fig. 1.2).



236 Figure 1.2: A string breaking and a creation of a new quark-antiquark pair [4].

237 On the other hand, for small  $r$ , an interaction between the quarks and gluons  
 238 is dominated by the Coulomb-like term  $-\frac{4}{3} \frac{\alpha_s}{r}$ . The coupling constant  $\alpha_s$  depends  
 239 on the four-momentum  $Q^2$  transferred in the interaction. This dependence is  
 240 presented in Fig. 1.3. The value  $\alpha_s$  decreases with increasing momentum trans-  
 241 fer and the interaction becomes weak for large  $Q^2$ , i.e.  $\alpha_s(Q) \rightarrow 0$ . Because  
 242 of the weakening of coupling constant, quarks at large energies (or small dis-  
 243 tances) are starting to behave like free particles. This phenomenon is known as  
 244 *asymptotic freedom*. The QCD potential also has temperature dependence - the  
 245 force strength "melts" with the temperature increase. Therefore the asymptotic  
 246 freedom is expected to appear in either the case of high baryon densities (small  
 247 distances between quarks) or very high temperatures. This temperature depend-  
 248 ence is illustrated in Fig. 1.4.

249 If the coupling constant  $\alpha_s$  is small, one can use perturbative methods to cal-  
 250 culate physical observables. Perturbative QCD (pQCD) successfully describes  
 251 hard processes (with large  $Q^2$ ), such as jet production in high energy proton-  
 252 antiproton collisions. The applicability of pQCD is defined by the *scale parameter*



Figure 1.3: The coupling parameter  $\alpha_s$  dependence on four-momentum transfer  $Q^2$  [5].

253  $\Lambda_{QCD} \approx 200$  MeV. If  $Q \gg \Lambda_{QCD}$  then the process is in the perturbative domain  
 254 and can be described by pQCD. A description of soft processes (when  $Q < 1$  GeV)  
 255 is a problem in QCD - perturbative theory breaks down at this scale. Therefore,  
 256 to describe processes with low  $Q^2$ , one has to use alternative methods like Lattice  
 257 QCD. Lattice QCD (LQCD) is non-perturbative implementation of a field theory  
 258 in which QCD quantities are calculated on a discrete space-time grid. LQCD al-  
 259 lows to obtain properties of matter in equilibrium, but there are some limitations.  
 260 Lattice QCD requires fine lattice spacing to obtain precise results - therefore large  
 261 computational resources are necessary. With the constant growth of computing  
 262 power this problem will become less important. The second problem is that lat-  
 263 tice simulations are possible only for baryon density  $\mu_B = 0$ . At  $\mu_B \neq 0$ , Lattice  
 264 QCD breaks down because of the sign problem. In QCD the thermodynamic  
 265 observables are related to the grand canonical partition function, which has a ba-  
 266 ryonic chemical potential  $\mu_B$  as a parameter. Therefore, the baryonic density can  
 267 be controlled by tuning the baryonic chemical potential. For fermions  $\mu_B$  can be  
 268 both positive and negative. For a particles with  $\mu_B$ , their antiparticles have chem-  
 269 ical potentials with opposite sign  $-\mu_B$ . Since at the early universe the number of  
 270 baryons and antibaryons were almost equal we can use  $\mu_B = 0$  to a very good  
 271 approximation [6].

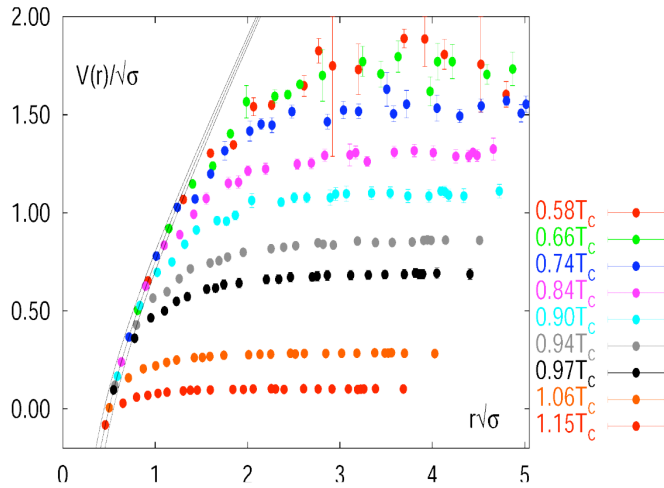


Figure 1.4: The QCD potential for a quark-antiquark pair as a function of distance for different temperatures. A value of a potential decreases with the temperature [4].

### 272 1.2.3 The quark-gluon plasma

273     The new state of matter in which quarks are no longer confined is known as  
 274     a *quark-gluon plasma* (QGP). The predictions coming from the discrete space-time  
 275     Lattice QCD calculations reveal a phase transition from the hadronic matter to  
 276     the quark-gluon plasma at the high temperatures and baryon densities. The res-  
 277     ults obtained from such calculations are shown on Fig. 1.5. The energy density  
 278      $\epsilon$  which is divided by  $T^4$  is a measure of the number of degrees of freedom in

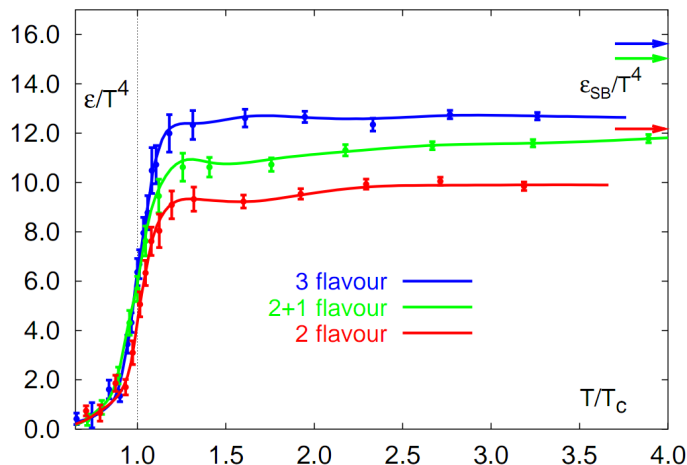


Figure 1.5: A number of degrees of freedom as a function of a temperature [7].

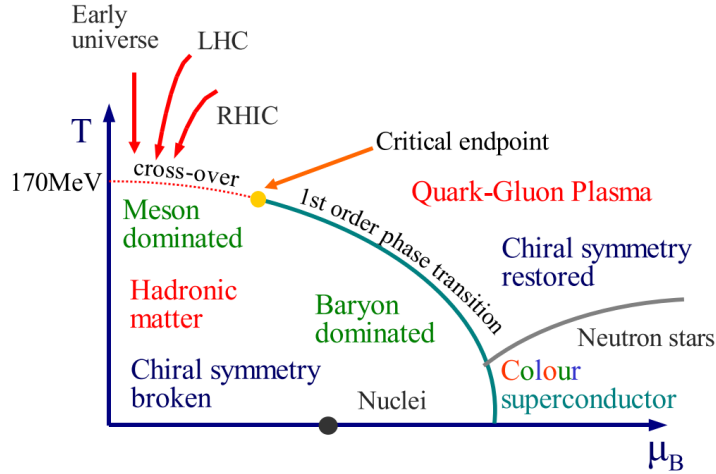


Figure 1.6: Phase diagram coming from the Lattice QCD calculations [8].

279 the system. One can observe significant rise of this value, when the temperature  
 280 increases past the critical value  $T_C$ . Such increase is signaling a phase transition  
 281 - the formation of QGP [8]. The values of the energy densities plotted in Fig. 1.5  
 282 do not reach the Stefan-Boltzmann limit  $\epsilon_{SB}$  (marked with arrows), which corre-  
 283 sponds to an ideal gas. This can indicate some residual interactions in the system.  
 284 According to the results from the RHIC<sup>2</sup>, the new phase of matter behaves more  
 285 like an ideal fluid, than like a gas [9].

286 One of the key questions, to which current heavy ion physics tries to find an  
 287 answer is the value of a critical temperature  $T_C$  as a function of a baryon chem-  
 288 ical potential  $\mu_B$  (baryon density), where the phase transition occurs. The results  
 289 coming from the Lattice QCD are presented in Fig. 1.6. The phase of matter in  
 290 which quarks and gluons are deconfined is expected to exist at large temperat-  
 291 ures. In the region of small temperatures and high baryon densities, a differ-  
 292 ent state is supposed to appear - a *colour superconductor*. The phase transition  
 293 between hadronic matter and the QGP is thought to be of 1<sup>st</sup> order at  $\mu_B \gg 0$ .  
 294 However as  $\mu_B \rightarrow 0$  quarks' masses become significant and a sharp transi-  
 295 tion transforms into a rapid but smooth cross-over. It is believed that in Pb-Pb colli-  
 296 sions observed at the LHC<sup>3</sup>, the created matter has high enough temperature to  
 297 be in the quark-gluon plasma phase, then cools down and converts into hadrons,  
 298 undergoing a smooth transition [8].

<sup>2</sup>Relativistic Heavy Ion Collider at Brookhaven National Laboratory in Upton, New York

<sup>3</sup>Large Hadron Collider at CERN, Geneva

### 299 1.3 Relativistic heavy ion collisions

#### 300 1.3.1 Stages of heavy ion collision

301 To create the quark-gluon plasma one has to achieve high enough temper-  
 302 atures and baryon densities. Such conditions can be recreated in the heavy ion  
 303 collisions at the high energies. The left side of the Figure 1.7 shows simplified

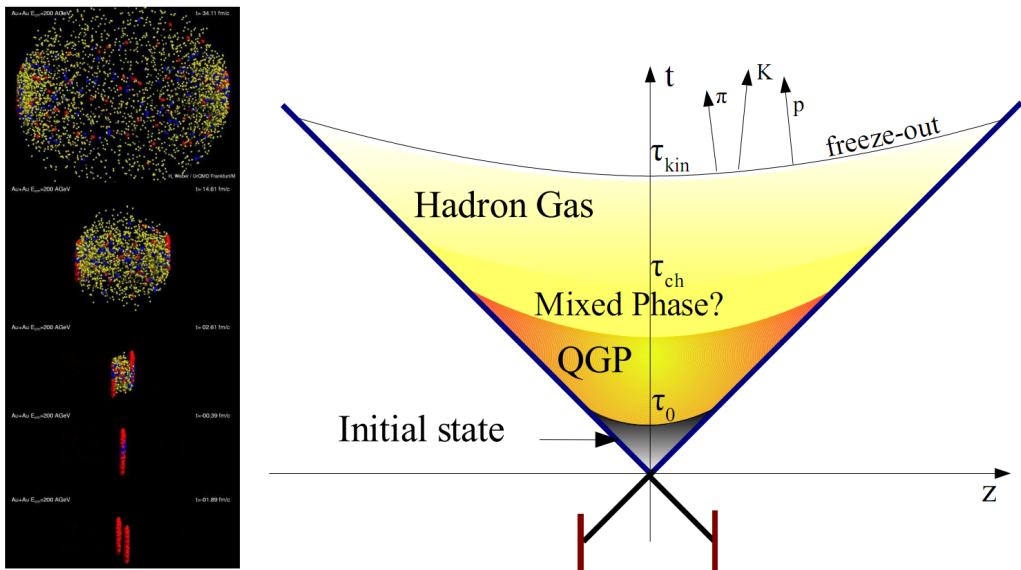


Figure 1.7: Left: stages of a heavy ion collision simulated in the UrQMD model.  
 Right: schematic view of a heavy ion collision evolution [8].

303 picture of a central collision of two highly relativistic nuclei in the centre-of-  
 304 mass reference frame. The colliding nuclei are presented as thin disks because  
 305 of the Lorentz contraction. In the central region, where the energy density is the  
 306 highest, a new state of matter - the quark-gluon plasma - is supposedly created.  
 307 Afterwards, the plasma expands ad cools down, quarks combine into hadrons  
 308 and their mutual interactions cease when the system reaches the *freeze-out* tem-  
 309 perature. Subsequently, produced free hadrons move towards the detectors.  
 310

311 On the right side of the Figure 1.7 a space-time evolution of a collision process  
 312 is presented, plotted in the light-cone variables ( $z$ ,  $t$ ). The two highly relativistic  
 313 nuclei are traveling basically along the light cone until they collide at the centre  
 314 of the diagram. Nuclear fragments emerge from the collision again along the  
 315 (forward) light cone, while the matter between fragmentation zones populates  
 316 the central region. This hot and dense matter is believed to be in the state of the  
 317 quark-gluon plasma. Several frameworks exist to describe this transition to the  
 318 QGP phase, for example: QCD string breaking, QCD parton cascades or colour  
 319 glass condensate evolving into glasma and later into quark-gluon plasma [10].

320 **String breaking** – In the string picture, the nuclei pass through each other forming colour strings. This is analogous to the situation depicted in the Fig 1.2 - the  
 321 colour string is created between quarks inside particular nucleons in nuclei. In  
 322 the next step strings decay / fragment forming quarks and gluons or directly  
 323 hadrons. This approach becomes invalid at very high energies, when the strings  
 324 overlap and cannot be treated as independent objects.

325 **Parton cascade** – The parton<sup>4</sup> cascade model is based on the pQCD. The colliding  
 326 nuclei are treated as clouds of quarks which penetrate through each other.  
 327 The key element of this method is the time evolution of the parton phase-space  
 328 distributions, which is governed by a relativistic Boltzmann equation with a col-  
 329 lision term that contains dominant perturbative QCD interactions. The bottleneck  
 330 of the parton cascade model is the low energies regime, where the  $Q^2$  is too small  
 331 to be described by the perturbative theory.

332 **Colour glass condensate** – The colour glass condensate assumes, that the had-  
 333 ion can be viewed as a tightly packed system of interacting gluons. The sat-  
 334 uration of gluons increases with energy, hence the total number of gluons may  
 335 increase without bound. Such a saturated and weakly coupled gluon system is  
 336 called a colour glass condensate. The fast gluons in the condensate are Lorentz  
 337 contracted and redistributed on the two very thin sheets representing two col-  
 338 liding nuclei. The sheets are perpendicular to the beam axis. The fast gluons  
 339 produce mutually orthogonal colour magnetic and electric fields, that only ex-  
 340 ist on the sheets. Immediately after the collision, i.e. just after the passage of  
 341 the two gluonic sheets through each other, the longitudinal electric and magnetic  
 342 fields are produced forming the *glasma*. The glasma fields decay through the  
 343 classical rearrangement of the fields into radiation of gluons. Also decays due to  
 344 the quantum pair creations are possible. In this way, the quark-gluon plasma is  
 345 produced.

346 Interactions within the created quark-gluon plasma bring the system into  
 347 the local statistical equilibrium, hence its further evolution can be described by  
 348 the relativistic hydrodynamics. The hydrodynamic expansion causes the sys-  
 349 tem to become more and more dilute. The phase transition from the quark-gluon  
 350 plasma to the hadronic gas occurs. Further expansion causes a transition from the  
 351 strongly interaction hadronic gas to weakly interacting system of hadrons which  
 352 move freely to the detectors. Such decoupling of hadrons is called the *freeze-out*.  
 353 The freeze-out can be divided into two phases: the chemical freeze-out and the  
 354 thermal one. The *chemical freeze-out* occurs when the inelastic collisions between  
 355 constituents of the hadron gas stop. As the system evolves from the chemical  
 356 freeze-out to the thermal freeze-out the dominant processes are elastic collisions  
 357 (such as, for example  $\pi + \pi \rightarrow \rho \rightarrow \pi + \pi$ ) and strong decays of heavier reso-  
 358 nances which populate the yield of stable hadrons. The *thermal freeze-out* is the  
 359 stage of the evolution of matter, when the strongly coupled system transforms  
 360 to a weakly coupled one (consisting of essentially free particles). In other words

---

<sup>4</sup>A parton is a common name for a quark and a gluon.

362 this is the moment, where the hadrons practically stop to interact. Obviously, the  
 363 temperatures corresponding to the two freeze-outs satisfy the condition

$$T_{chem} > T_{therm}, \quad (1.2)$$

364 where  $T_{chem}$  (inferred from the ratios of hadron multiplicities) is the temperature  
 365 of the chemical freeze-out, and  $T_{therm}$  (obtained from the investigation of the  
 366 transverse-momentum spectra) is the temperature of the thermal freeze-out [10].

### 367 1.3.2 QGP signatures

368 The quark-gluon plasma is a very short living and unstable state of matter.  
 369 One cannot investigate the properties of a plasma and confirm its existence directly.  
 370 Hence, the several experimental effects were proposed as QGP signatures,  
 371 some of them have been already observed in heavy ion experiments [8]. As matter  
 372 created in the heavy ions collisions is supposed to behave like a fluid, one  
 373 should expect appearance of collective behaviour at small transverse momenta  
 374 - so called *elliptic flow* and *radial flow*. The next signal is the temperature range  
 375 obtained from the measurements of *direct photons*, which gives us information,  
 376 that the system created in heavy ion collisions is far above the critical temperat-  
 377 ure obtained from the LQCD calculations. The *puzzle in the di-lepton spectrum* can  
 378 be explained by the modification of spectral shape of vector mesons (mostly  $\rho$   
 379 meson) in the presence of a dense medium. This presence of a medium can also  
 380 shed light on the *jet quenching* phenomenon - the suppression occurrence in the  
 381 high  $p_T$  domain.

#### 382 Elliptic flow

383 In a non-central heavy ion collisions, created region of matter has an almond  
 384 shape with its shorter axis in the *reaction plane* (Fig. 1.8). The pressure gradient

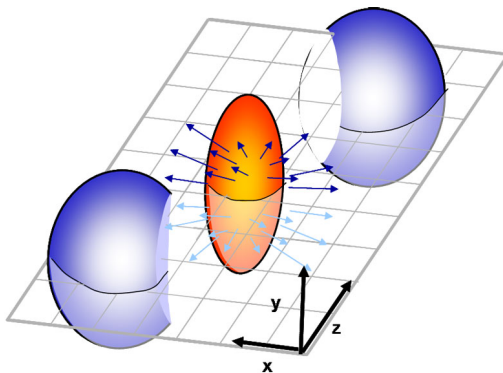


Figure 1.8: Overlapping region which is created in heavy ion collisions has an almond shape. Visible x-z plane is a *reaction plane*. The x-y plane is a *transverse plane*. The z is a direction of the beam [11].

is much larger in-plane rather than out-of-plane. This causes larger acceleration and transverse velocities in-plane rather than out-of-plane. Such differences can be investigated by studying the distribution of particles with respect to the reaction plane orientation [12]:

$$E \frac{d^3 N}{dp^3} = \frac{1}{2\pi} \frac{d^2 N}{p_T dp_T dy} (1 + 2v_1 \cos(\phi) + 2v_2 \cos(2\phi) + \dots), \quad (1.3)$$

where  $\phi$  is the angle between particle transverse momentum  $p_T$  (a momentum projection on a transverse plane) and the reaction plane,  $N$  is a number of particles and  $E$  is an energy of a particle. The  $y$  variable is *rapidity* defined as:

$$y = \frac{1}{2} \ln \left( \frac{E + p_L}{E - p_L} \right), \quad (1.4)$$

where  $p_L$  is a longitudinal component of a momentum (parallel to the beam direction). The  $v_n$  coefficients indicate the shape of a system. For the most central collisions ( $b = 0$  - see Fig. 1.9) all coefficients vanish  $\sum_{n \in N_+} v_n = 0$  (the overlapping region has the spherical shape). The Fourier series elements in the parentheses in Eq. 1.3 represent different kinds of flow. The first value: "1" represents the *radial flow* - an isotropic flow in every direction. Next coefficient  $v_1$  is responsible for *direct flow*. The  $v_2$  coefficient is a measure of elliptic anisotropy (*elliptic flow*). The  $v_2$  has to build up in the early stage of a collision - later the system becomes too dilute: space asymmetry and the pressure gradient vanish. Therefore the observation of elliptic flow means that the created matter was in fact a strongly interacting matter.

The  $v_2$  coefficient was measured already at CERN SPS, LHC and RHIC. For the first time hydrodynamics successfully described the collision dynamics as the

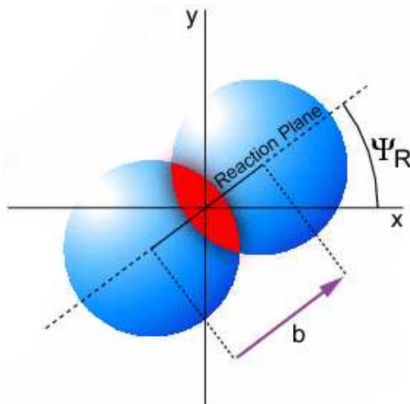


Figure 1.9: Cross-section of a heavy ion collision in a transverse plane. The  $b$  parameter is an *impact parameter* - a distance between centers of nuclei during a collision. An impact parameter is related with the centrality of a collision and a volume of the quark-gluon plasma [12].

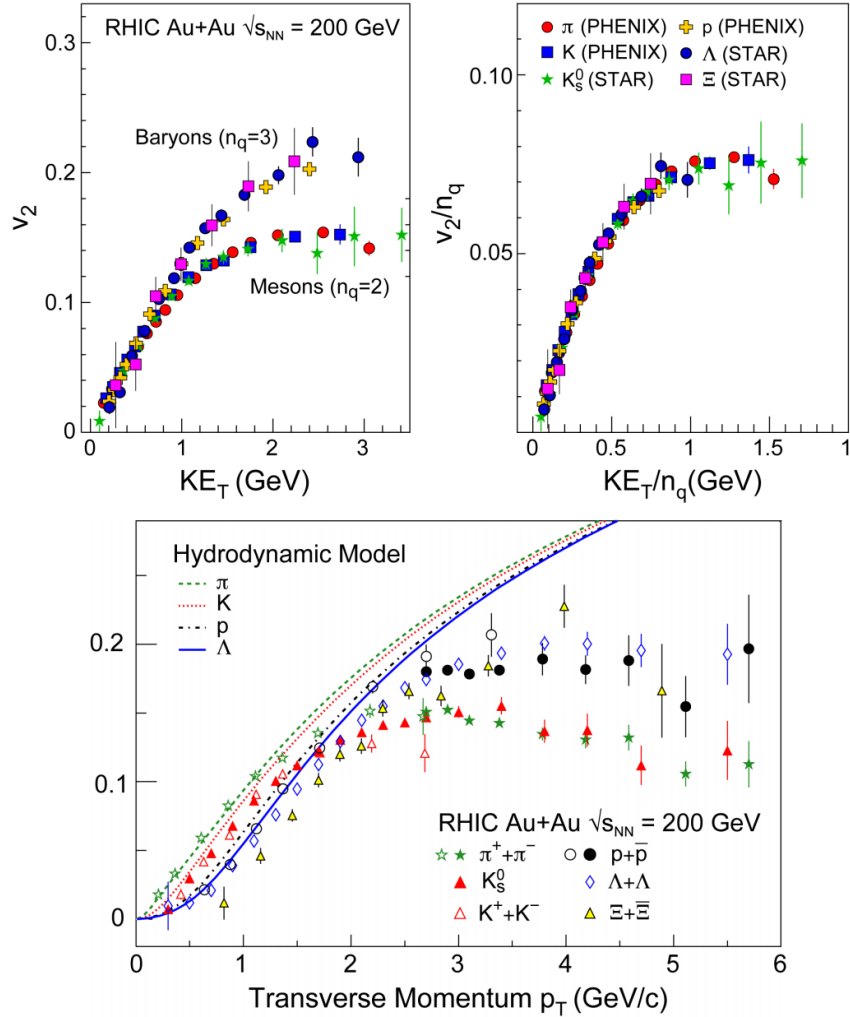


Figure 1.10: *Lower:* The elliptic flow  $v_2$  follows the hydrodynamical predictions for an ideal fluid perfectly. Note that > 99% of all final hadrons have  $p_T < 1.5 \text{ GeV}/c$ . *Upper left:* The  $v_2$  plotted versus transverse kinetic energy  $KE_T = m_T - m_0 = \sqrt{p_T^2 + m_0^2} - m_0$ . The  $v_2$  follows different universal curves for mesons and baryons. *Upper right:* When scaled by the number of valence quarks, the  $v_2$  follows the same universal curve for all hadrons and for all values of scaled transverse kinetic energy [13].

measured  $v_2$  reached hydrodynamic limit (Fig. 1.10). As expected, there is a mass ordering of  $v_2$  as a function of  $p_T$  (lower plot in the Fig. 1.10) with pions having the largest and protons the smallest anisotropy. In the upper plots in the Fig. 1.10 there is a  $v_2$  as a function of transverse kinetic energy. The left plot shows two universal trend lines for baryons and mesons. After the scaling of  $v_2$  and the

410 kinetic energy by the number of valence quarks, all of the hadrons follow the  
 411 same universal curve. Those plots show that strong collectivity is observed in  
 412 heavy ion collisions.

413 **Transverse radial flow**

414 Elliptic flow described previously is caused by the pressure gradients which  
 415 must also produce a more simple collective behaviour of matter - a movement  
 416 inside-out, called radial flow. Particles are pushed to higher momenta and they  
 417 move away from the center of the collision. A source not showing collective  
 418 behaviour, like pp collisions, produces particle spectra that can be fitted by a  
 419 power-law [8]:

$$\frac{1}{2\pi p_T} \frac{d^2 N}{dp_T d\eta} = C \left( 1 + \frac{p_T}{p_0} \right)^{-n} . \quad (1.5)$$

420 The  $\eta$  variable is *pseudorapidity* defined as follows:

$$\eta = \frac{1}{2} \ln \left( \frac{p + p_L}{p - p_L} \right) = -\ln \left( \frac{\theta}{2} \right) , \quad (1.6)$$

where  $\theta$  is an emission angle  $\cos \theta = p_L/p$ .

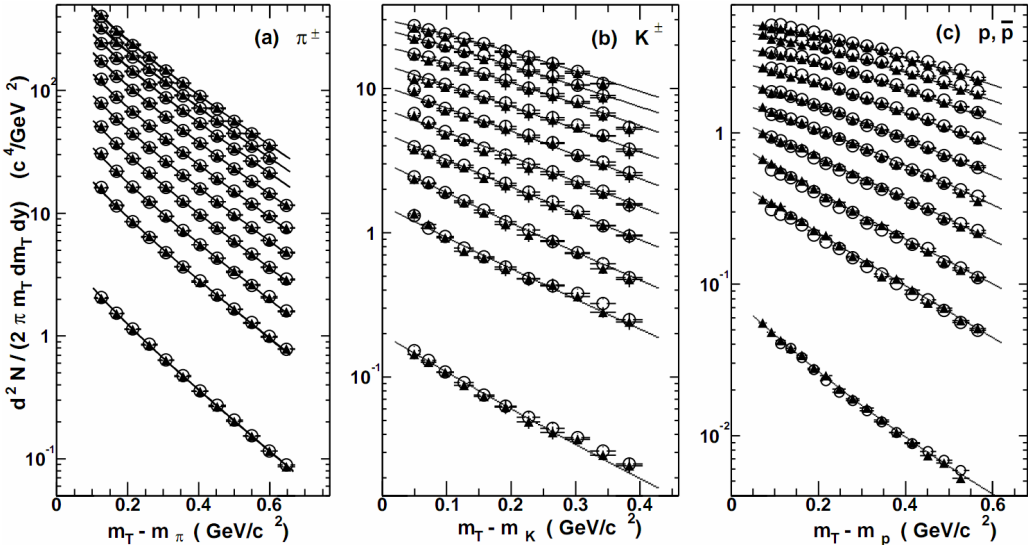


Figure 1.11: Invariant yield of particles versus transverse mass  $m_T = \sqrt{p_T^2 + m_0^2}$  for  $\pi^\pm$ ,  $K^\pm$ ,  $p$  and  $\bar{p}$  at mid-rapidity for p+p collisions (bottom) and Au+Au events from 70-80% (second bottom) to 0-5% (top) centrality [14].

421  
 422 The hydrodynamical expansion of a system gives the same flow velocity kick  
 423 for different kinds of particles - ones with bigger masses will gain larger  $p_T$  boost.  
 424 This causes increase of the yield of particles with larger transverse momenta. In

the invariant yield plots one can observe the decrease of the slope parameter, especially for the heavier hadrons. This is presented in the Fig. 1.11. The most affected spectra are ones of kaons (b) and protons (c). One can notice decrease of the slope parameter for heavy ion collisions (plots from second bottom to top) comparing to the proton-proton collisions (bottom ones), where no boost from radial flow should occur [8].

Another signature of a transverse radial flow is a dependence of HBT radii on a pair transverse momentum. Detailed description of this effect is presented in the Section 3.4.

#### 434 Direct photons

The direct photons are photons, which are not coming from the final state hadrons decays. Their sources can be various interaction from charged particles created in the collision, either at the partonic or at the hadronic level. Direct photons are considered to be an excellent probe of the early stage of the collision. This is because their mean free path is very large when compared to the size of created system in the collision. Thus photons created at the early stage leave the system without suffering any interaction and retain information about this stage, in particular about its temperature.

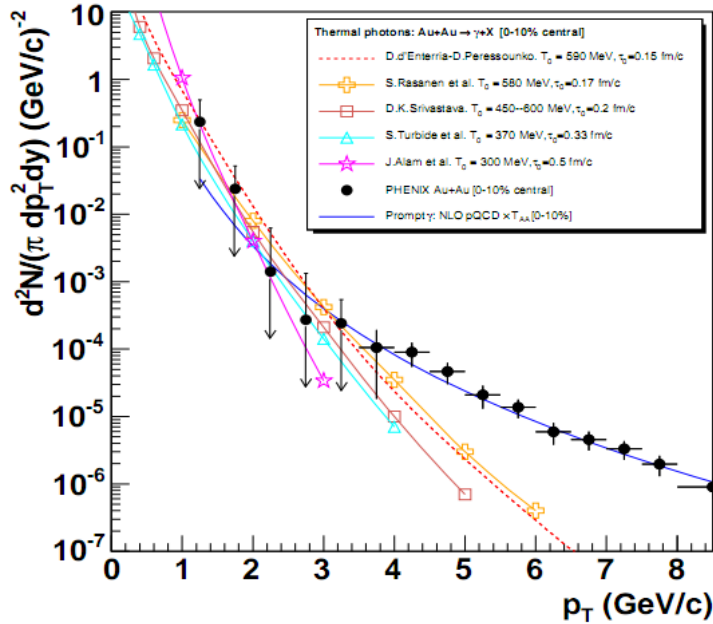


Figure 1.12: Thermal photons spectra for the central Au+Au collisions at  $\sqrt{s_{NN}} = 200$  GeV computed within different hydrodynamical models compared with the pQCD calculations (solid line) and experimental data from PHENIX (black dots) [15].

One can distinguish two kinds of direct photons: *thermal* and *prompt*. Thermal photons can be emitted from the strong processes in the quark-gluon plasma involving quarks and gluons or hot hadronic matter (e.g. processes:  $\pi\pi \rightarrow \rho\gamma$ ,  $\pi\rho \rightarrow \pi\gamma$ ). Thermal photons can be observed in the low  $p_T$  region. Prompt photons are believed to come from “hard” collisions of initial state partons belonging to the colliding nuclei. The prompt photons can be described using the pQCD. They will dominate the high  $p_T$  region. The analysis of transverse momentum of spectra of direct photons revealed, that the temperature of the source of thermal photons produced in heavy ion collisions at RHIC is in the range 300–600 MeV (Fig. 1.12). Hence the direct photons had to come from a system whose temperature is far above from the critical temperature for QGP creation.

#### Puzzle in di-lepton mass spectrum

The invariant mass spectra (Fig. 1.13) of lepton pairs reveal many peaks corresponding to direct decays of various mesons into a lepton pair. The continuous background in this plot is caused by the decays of hadrons into more than two leptons (including so-called *Dalitz decays* into a lepton pair and a photon). Particular hadron decay channels, which contribute to this spectrum are shown

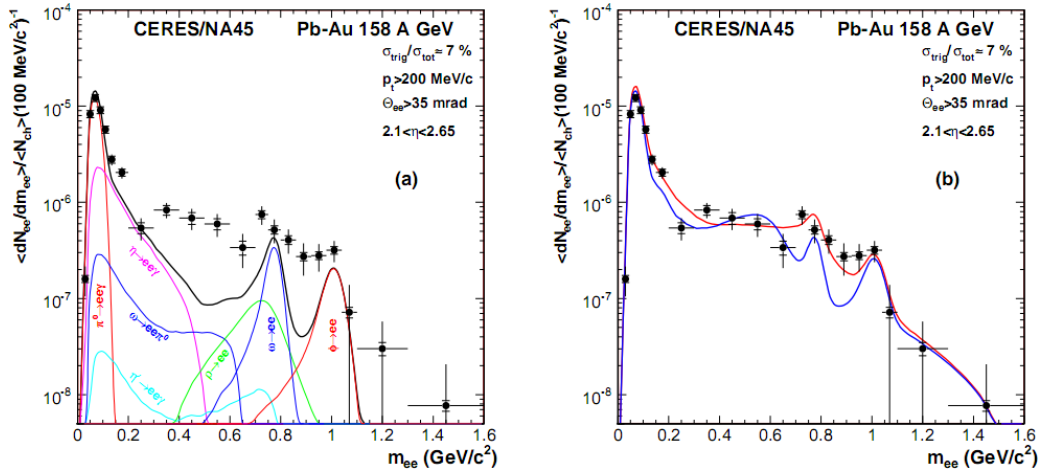


Figure 1.13: Left: Invariant mass spectrum of  $e^+ - e^-$  pairs in  $Pb+Au$  collisions at  $158A$  GeV compared to the sum coming from the hadron decays predictions. Right: The expectations coming from model calculations assuming a dropping of the  $\rho$  mass (blue) or a spread of the  $\rho$  width in the medium (red) [16].

in Fig. 1.13 with the coloured lines and their sum with the black one. The sum (called *the hadronic cocktail*) of various components describes experimental spectra coming from the simple collisions (like  $p+p$  or  $p+A$ ) quite well with the statistical and systematical uncertainties [9]. This situation is different considering more complicated systems i.e.  $A+A$ . Spectra coming from  $Pb+Au$  collisions are presented on the plots in the Fig. 1.13. The “hadronic cocktail” does not describe

the data, in the mass range between the  $\pi$  and the  $\rho$  mesons a significant excess of electron pairs over the calculated sum is observed. Theoretical explanation of this phenomenon assumes modification of the spectral shape of vector mesons in a dense medium. Two different interpretations of this increase were proposed: a decrease of meson mass with the medium density and increase of the meson width in the dense medium. In principle, one could think of simultaneous occurrence of both effects: mass shift and resonance broadening. Experimental results coming from the CERES disfavour the mass shift hypothesis indicating only broadening of resonance peaks (Fig. 1.13b) [9].

#### 475 Jet quenching

A jet is defined as a group of particles with close vector momenta and high energies. It has its beginning when the two partons are going in opposite directions and have energy big enough to produce new quark-antiquark pair and then radiate gluons. This process can be repeated many times and it results in two back-to-back jets of hadrons. It has been found that jets in the opposite hemisphere (*away-side jets*) show a very different pattern in d+Au and Au+Au collisions. This is shown in the azimuthal correlations in the Fig. 1.14. In d+Au collisions, like in p+p, a pronounced away-side jet appears around  $\Delta\phi = \pi$ , exactly opposite to the trigger jet, which is typical for di-jet events. In central Au+Au collisions the away-side jet is suppressed. When the jet has its beginning near the surface of the quark-gluon plasma, one of the jets (*near-side jet*) leaves the system almost without any interactions. This jet is visible on the correlation plot as a high peak

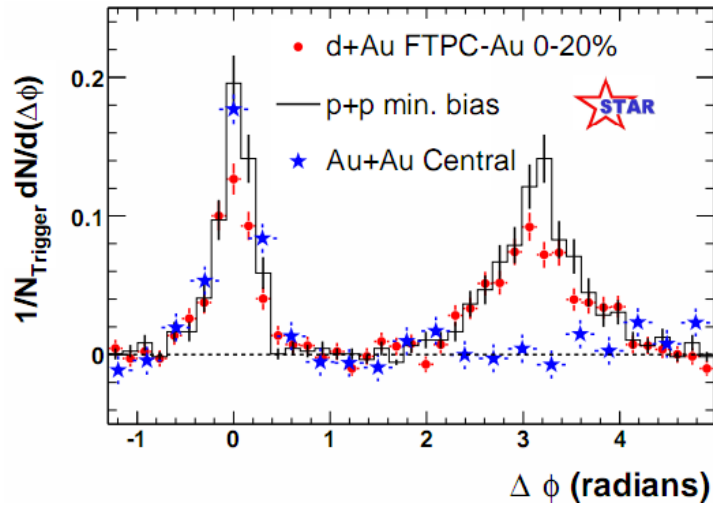


Figure 1.14: Azimuthal angle difference  $\Delta\phi$  distributions for different colliding systems at  $\sqrt{s_{NN}} = 200$  GeV. Transverse momentum cut:  $p_T > 2$  GeV. For the Au+Au collisions the away-side jet is missing [17].

488 at  $\Delta\phi = 0$ . However, the jet moving towards the opposite direction has to penetrate  
489 a dense medium. The interaction with the plasma causes energy dissipation  
490 of particles and is visible on an azimuthal correlation plot as a disappearance of  
491 the away-side jet [9].

492 **Chapter 2**

493 **Therminator model**

494     THERMINATOR [18] is a Monte Carlo event generator designed to investigate  
495     the particle production in the relativistic heavy ion collisions. The functionality  
496     of the code includes a generation of the stable particles and unstable resonances  
497     at the chosen hypersurface model. It performs the statistical hadronization which  
498     is followed by space-time evolution of particles and the decay of resonances. The  
499     key element of this method is an inclusion of a complete list of hadronic reso-  
500     nances, which contribute very significantly to the observables. The second version  
501     of THERMINATOR [19] comes with a possibility to incorporate any shape of freeze-  
502     out hypersurface and the expansion velocity field, especially those generated ex-  
503     ternally with various hydrodynamic codes.

504 **2.1 (3+1)-dimensional viscous hydrodynamics**

505     Most of the relativistic viscous hydrodynamic calculations are done in  
506     (2+1)-dimensions. Such simplification assumes boost-invariance of a matter  
507     created in a collision. Experimental data reveals that no boost-invariant region is  
508     formed in the collisions [20]. Hence, for the better description of created system  
509     a (3+1)-dimensional model is required.

510     In the four dimensional relativistic dynamics one can describe a system  
511     using a space-time four-vector  $x^\nu = (ct, x, y, z)$ , a velocity four-vector  
512      $u^\nu = \gamma(c, v_x, v_y, v_z)$  and a energy-momentum tensor  $T^{\mu\nu}$ . The particular  
513     components of  $T^{\mu\nu}$  have a following meaning:

- 514       •  $T^{00}$  - an energy density,
- 515       •  $cT^{0\alpha}$  - an energy flux across a surface  $x^\alpha$ ,
- 516       •  $T^{\alpha 0}$  - an  $\alpha$ -momentum flux across a surface  $x^\alpha$  multiplied by  $c$ ,
- 517       •  $T^{\alpha\beta}$  - components of momentum flux density tensor,

518 where  $\gamma = (1 - v^2/c^2)^{-1/2}$  is Lorentz factor and  $\alpha, \beta \in \{1, 2, 3\}$ . Using  $u^\nu$  one can  
 519 express  $T^{\mu\nu}$  as follows [21]:

$$T_0^{\mu\nu} = (e + p)u^\mu u^\nu - pg^{\mu\nu} \quad (2.1)$$

520 where  $e$  is an energy density,  $p$  is a pressure and  $g^{\mu\nu}$  is an inverse metric tensor:

$$g^{\mu\nu} = \begin{bmatrix} 1 & 0 & 0 & 0 \\ 0 & -1 & 0 & 0 \\ 0 & 0 & -1 & 0 \\ 0 & 0 & 0 & -1 \end{bmatrix}. \quad (2.2)$$

521 The presented version of energy-momentum tensor (Eq. 2.1) can be used to de-  
 522 scribe dynamics of a perfect fluid. To take into account influence of viscosity,  
 523 one has to apply the following corrections coming from shear  $\pi^{\mu\nu}$  and bulk  $\Pi$   
 524 viscosities [22]:

$$T^{\mu\nu} = T_0^{\mu\nu} + \pi^{\mu\nu} + \Pi(g^{\mu\nu} - u^\mu u^\nu). \quad (2.3)$$

525 The stress tensor  $\pi^{\mu\nu}$  and the bulk viscosity  $\Pi$  are solutions of dynamical equa-  
 526 tions in the second order viscous hydrodynamic framework [21]. The compari-  
 527 son of hydrodynamics calculations with the experimental results reveal, that the  
 528 shear viscosity divided by entropy  $\eta/s$  has to be small and close to the AdS/CFT  
 529 estimate  $\eta/s = 0.08$  [22, 23]. The bulk viscosity over entropy value used in calcu-  
 530 lations is  $\zeta/s = 0.04$  [22].

531 When using  $T^{\mu\nu}$  to describe system evolving close to local thermodynamic  
 532 equilibrium, relativistic hydrodynamic equations in a form of:

$$\partial_\mu T^{\mu\nu} = 0 \quad (2.4)$$

533 can be used to describe the dynamics of the local energy density, pressure and  
 534 flow velocity.

535 Hydrodynamic calculations are starting from the Glauber<sup>1</sup> model initial con-  
 536 ditions. The collective expansion of a fluid ends at the freeze-out hypersurface.  
 537 That surface is usually defined as a constant temperature surface, or equivalently  
 538 as a cut-off in local energy density. The freeze-out is assumed to occur at the  
 539 temperature  $T = 140$  MeV.

## 540 2.2 Statistical hadronization

541 Statistical description of heavy ion collision has been successfully used to  
 542 quantitatively describe the *soft* physics, i.e. the regime with the transverse mo-  
 543 mentum not exceeding 2 GeV. The basic assumption of the statistical approach of  
 544 evolution of the quark-gluon plasma is that at some point of the space-time evol-  
 545 ution of the fireball, the thermal equilibrium is reached. When the system is in the

---

<sup>1</sup>The Glauber Model is used to calculate “geometrical” parameters of a collision like an impact parameter, number of participating nucleons or number of binary collisions.

546 thermal equilibrium the local phase-space densities of particles follow the Fermi-  
 547 Dirac or Bose-Einstein statistical distributions. At the end of the plasma expan-  
 548 sion, the freeze-out occurs. The freeze-out model incorporated in THERMINATOR  
 549 assumes, that chemical and thermal freeze-outs occur at the same time.

550 **2.2.1 Cooper-Frye formalism**

551 The result of the hydrodynamic calculations is the freeze-out hyper-  
 552 surface  $\Sigma^\mu$ . A three-dimensional element of the surface is defined as [19]

$$553 \quad d\Sigma_\mu = \epsilon_{\mu\alpha\beta\gamma} \frac{\partial x^\alpha}{\partial \alpha} \frac{\partial x^\beta}{\partial \beta} \frac{\partial x^\gamma}{\partial \gamma} d\alpha d\beta d\gamma, \quad (2.5)$$

554 where  $\epsilon_{\mu\alpha\beta\gamma}$  is the Levi-Civita tensor and the variables  $\alpha, \beta, \gamma \in \{1, 2, 3\}$  are used  
 555 to parametrize the three-dimensional freeze-out hypersurface in the Minkowski  
 556 four-dimensional space. The Levi-Civita tensor is equal to 1 when the indices  
 557 form an even permutation (eg.  $\epsilon_{0123}$ ), to -1 when the permutation is odd (e.g.  
 558  $\epsilon_{2134}$ ) and has a value of 0 if any index is repeated. Therefore [19],

$$559 \quad d\Sigma_0 = \begin{vmatrix} \frac{\partial x}{\partial \alpha} & \frac{\partial x}{\partial \beta} & \frac{\partial x}{\partial \gamma} \\ \frac{\partial y}{\partial \alpha} & \frac{\partial y}{\partial \beta} & \frac{\partial y}{\partial \gamma} \\ \frac{\partial z}{\partial \alpha} & \frac{\partial z}{\partial \beta} & \frac{\partial z}{\partial \gamma} \end{vmatrix} d\alpha d\beta d\gamma \quad (2.6)$$

560 and the remaining components are obtained by cyclic permutations of  $t, x, y$   
 561 and  $z$ .

One can obtain the number of hadrons produced on the hypersurface  $\Sigma^\mu$  from  
 the Cooper-Frye formalism. The following integral yields the total number of  
 created particles [19]:

$$562 \quad N = (2s + 1) \int \frac{d^3 p}{(2\pi)^3 E_p} \int d\Sigma_\mu p^\mu f(p_\mu u^\mu), \quad (2.7)$$

563 where  $f(p_\mu u^\mu)$  is the phase-space distribution of particles (for stable ones and res-  
 564 onances). One can simply derive from Eq. 2.7, the dependence of the momentum  
 565 density [24]:

$$566 \quad E \frac{d^3 N}{dp^3} = \int d\Sigma_\mu f(p_\mu u^\mu) p^\mu. \quad (2.8)$$

567 The momentum distribution  $f$  contains non-equilibrium corrections:

$$568 \quad f = f_0 + \delta f_{shear} + \delta f_{bulk}, \quad (2.9)$$

569 where

$$570 \quad f_0(p_\mu u^\mu) = \left\{ \exp \left[ \frac{p_\mu u^\mu - (B\mu_B + I_3\mu_{I_3} + S\mu_S + C\mu_C)}{T} \right] \pm 1 \right\}^{-1}. \quad (2.10)$$

566 In case of fermions, in the Eq. 2.10 there is a plus sign and for bosons, minus  
 567 sign respectively. The thermodynamic quantities appearing in the  $f_0(\cdot)$  are  $T$  -  
 568 temperature,  $\mu_B$  - baryon chemical potential,  $\mu_{I_3}$  - isospin chemical potential,  $\mu_S$   
 569 - strange chemical potential,  $\mu_C$  - charmed chemical potential and the  $s$  is a spin of  
 570 a particle. The hydrodynamic calculations yield the flow velocity at freeze-out as  
 571 well as the stress and bulk viscosity tensors required to calculate non-equilibrium  
 572 corrections to the momentum distribution used in Eq. 2.7. The term coming from  
 573 shear viscosity has a form [22]

$$\delta f_{shear} = f_0(1 \pm f_0) \frac{1}{2T^2(e + p)} p^\mu p^\nu \pi_{\mu\nu} \quad (2.11)$$

574 and bulk viscosity

$$\delta f_{bulk} = C f_0(1 \pm f_0) \left( \frac{(u^\mu p_\mu)^2}{3u^\mu p_\mu} - c_s^2 u^\mu p_\mu \right) \Pi \quad (2.12)$$

575 where  $c_s$  is sound velocity and

$$\frac{1}{C} = \frac{1}{3} \frac{1}{(2\pi)^3} \sum_{hadrons} \int d^3 p \frac{m^2}{E} f_0(1 \pm f_0) \left( \frac{p^2}{3E} - c_s^2 E \right). \quad (2.13)$$

### 576 2.3 Events generation procedure

577 The equations presented in the previous section are directly used in the  
 578 THERMINATOR to generate the primordial hadrons (created during freeze-out)  
 579 with the Monte-Carlo method. This procedure consists of 3 main steps, where  
 580 the first two are performed only once per given parameter set. After the  
 581 generation of primordial particles, the cascade decay of unstable resonances is  
 582 performed.

#### 583 Determination of a maximum of an integrand

584 In order to generate particles through a Monte Carlo method, the maximum  
 585 value of the distribution in the right-hand-side of Eq. 2.7 must be known. To find  
 586 this number, THERMINATOR performs a generation of a sample consisting of a  
 587 large number of particles. For each particle the value of a distribution is cal-  
 588 culated and the maximum value  $f_{max}$  of the sample is stored. A large enough  
 589 sample of particles guarantees that  $f_{max}$  found in this procedure is a good es-  
 590 timate of the maximum value of a distribution in Eq. 2.7. This maximum value  
 591 depends on a particle type and values of parameters, but does not change from  
 592 event to event, hence this procedure is performed once, at the beginning of the  
 593 events generation [18].

594 **Multiplicity calculation**

595 In order to generate events, a multiplicity of each particle must be known.  
 596 The multiplicities are obtained through a numerical integration of distribution  
 597 functions (Eq. 2.7) in the given integration ranges determined by the model para-  
 598 meters. The multiplicities also depend only on the model parameters and they  
 599 are also only calculated once at the beginning of the event generation [18].

600 **Events and particles generation**

601 Each of the events produced by THERMINATOR are generated separately. At  
 602 first, the multiplicities for each of particle type are generated as random numbers  
 603 from a Poisson distribution, with the mean being the average particle multipli-  
 604 city determined in the previous step. Then the program proceeds to generate  
 605 particles from the heaviest to the lightest particle type. In essence, this procedure  
 606 is a generation of the set of six random numbers: three components of particle's  
 607 momentum ( $p_x, p_y, p_z$ ) and three parameters providing space-time coordinates  
 608 on a freeze-out hypersurface ( $\zeta, \phi_s, \theta$ ). Event generation procedure is based on  
 609 von Neumann's acceptance-rejection algorithm. Firstly, the integrand in Eq. 2.7  
 610 is calculated using given set of numbers. Subsequently, a random number from  
 611 uniform distribution over  $[0; f_{max}]$  is compared to the value of integrand. If it  
 612 is lower, then the set of numbers is stored as actual particle. If this condition  
 613 was not satisfied, a new set is generated. This procedure is repeated until the  
 614 determined number of particles of each kind is generated. At this point all prim-  
 615 ordial particles (stable and resonances) have been generated and stored in the  
 616 event [18].

617 **Decays of unstable particles**

618 In the next step of event generation, a simulation of decays of unstable res-  
 619 onances is performed. A particle is considered as unstable when it has non-zero  
 620 width  $\Gamma$  defined in the input files of THERMINATOR. The decays proceed sequen-  
 621 tially from the heaviest particles to the lightest. Unstable products of decays are  
 622 added to the particles generated in the current event and are processed in the  
 623 subsequent steps. If a particle has several decay channels, one of them is selec-  
 624 ted randomly with the appropriate probability corresponding to the branching  
 625 ratio provided in the input files. THERMINATOR in the hadronic cascade process  
 626 performs two-body and three-body decays.

627 At the beginning of the cascade decay, the lifetime  $\tau$  of a particle with mass  
 628  $M$ , moving with the four-momentum  $p^\mu$ , is generated randomly according to the  
 629 exponential decay law  $\exp(-\Gamma\tau)$ . When the lifetime is known, the point of its  
 630 decay is calculated as [18]:

$$x_{decay}^\mu = x_{origin}^\mu + \frac{p^\mu}{M}\tau, \quad (2.14)$$

631 where  $x_{\text{origin}}^\mu$  is a space-time position, where the unstable particle was generated.  
 632 At the  $x_{\text{decay}}^\mu$  point decay occurs and daughter particles with energies and mo-  
 633 ments determined by the conservation laws are generated. Fig. 2.1 illustrates the  
 cascade decay process [18].

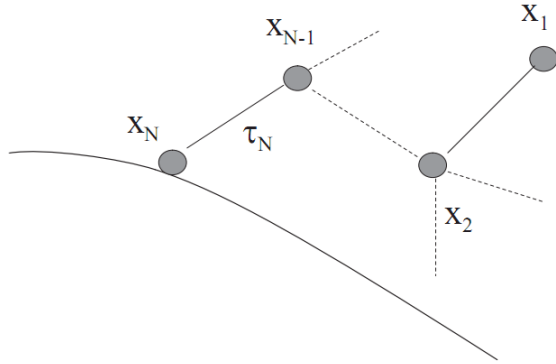


Figure 2.1: The cascade decay in the single freeze-out model. An unstable resonance  $x_N$  is formed at the freeze-out hypersurface and travels for the time  $\tau_N$  depending on its lifetime and decays. If the products are also resonances ( $x_{N-1}$ ,  $x_2$ ) they decay further until the stable particles are formed ( $x_1$ ) [18].

635 **Chapter 3**

636 **Particle interferometry**

637 Two-particle interferometry (also called *femtoscopy*) gives a possibility to  
638 investigate space-time characteristics of the particle-emitting source created  
639 in heavy ion collisions. Through the study of particle correlations, their  
640 momentum distributions can be used to obtain information about the spatial  
641 extent of the created system. Using this method, one can measure sizes of the  
642 order of  $10^{-15}$  m and time of the order of  $10^{-23}$  s.

643 **3.1 HBT interferometry**

644 In the 1956 Robert Hanbury Brown and Richard Q. Twiss proposed a method  
645 which allowed to investigate angular dimensions of stars through analysis of  
646 interference between photons. They performed a measurement of the intensity  
647 of a beam of light coming from a star using two separated detectors. In a sig-  
648 nal plotted as a function of distance between detectors an interference effect was  
649 observed, revealing a positive correlation, despite the fact that no phase inform-  
650 ation was collected. Hanbury, Brown and Twiss used this interference signal to  
651 calculate the angular size of a star with the excellent resolution. This method was  
652 designed to be used in astronomy, however HBT interferometry can be used also  
653 to measure extent of any emitting source. Therefore it was adapted to heavy ion  
654 collisions to investigate dimensions of a particle-emitting source [8].

655 **3.2 Theoretical approach**

656 Intensity interferometry in heavy ion physics uses similar mathematical form-  
657 alism as the astronomy HBT measurement. The difference between them is that  
658 femtoscopy uses a two-particle relative momentum and yields the space-time  
659 picture of a source, whereas the latter method uses the distance between detect-  
660 ors to calculate angular size of the star.

661 **3.2.1 Conventions used**

662 In heavy ion collisions to describe particular directions, components of mo-  
 663 mentum and location of particles, one uses naming convention called the Bertsch-  
 Pratt coordinate system. This system is presented in the Fig. 3.1. The three dir-

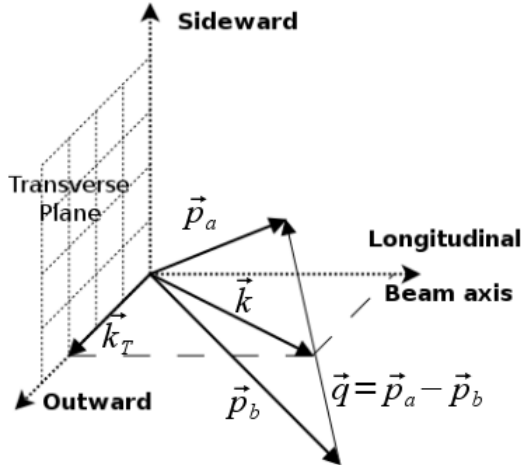


Figure 3.1: Bertsch-Pratt direction naming convention used in heavy ion collision.

664  
 665 ections are called *longitudinal*, *outward* and *sideward*. The longitudinal direction  
 666 is parallel to the beam axis. The plane perpendicular to the beam axis is called  
 667 a *transverse plane*. A projection of a particle pair momentum  $\mathbf{k} = (\mathbf{p}_a + \mathbf{p}_b)/2$   
 668 on a transverse plane (a *transverse momentum*  $\mathbf{k}_T$ ) determines *outward* direction:  
 669  $(\mathbf{k})_{out} = \mathbf{k}_T$ . A direction perpendicular to the longitudinal and outward is called  
 670 *sideward*.

671 A particle pair is usually described using two coordinate systems. The first  
 672 one, *Longitudinally Co-Moving System* (LCMS) is moving along the particle pair  
 673 with the longitudinal direction, in other words, the pair longitudinal momentum  
 674 vanishes:  $(\mathbf{p}_a)_{long} = -(\mathbf{p}_b)_{long}$ . The second system is called *Pair Rest Frame* (PRF).  
 675 In the PRF the centre of mass rests:  $\mathbf{p}_a = -\mathbf{p}_b$ . Variables which are expressed in  
 676 the PRF are marked with a star (e.g.  $\mathbf{k}^*$ ).

The transition of space-time coordinates from LCMS to PRF is simply  
 a boost along the outward direction, with the transverse velocity of the  
 pair  $\beta_T = (\mathbf{v}/c)_{out}$  [25]:

$$r_{out}^* = \gamma_t(r_{out} - \beta_T \Delta t) \quad (3.1)$$

$$r_{side}^* = r_{side} \quad (3.2)$$

$$r_{long}^* = r_{long} \quad (3.3)$$

$$\Delta t^* = \gamma_T(\Delta t - \beta_T r_{out}), \quad (3.4)$$

677 where  $\gamma_T = (1 - \beta_T^2)^{-1/2}$  is the Lorentz factor. However, in calculations performed

in this work the equal time approximation is used, which assumes that particles in a pair were produced at the same time in PRF - the  $\Delta t^*$  is neglected.

The most important variables used to describe particle pair are their total momentum  $\mathbf{P} = \mathbf{p}_a + \mathbf{p}_b$  and relative momentum  $\mathbf{q} = \mathbf{p}_a - \mathbf{p}_b$ . In the PRF one has  $\mathbf{q} = 2\mathbf{k}^*$ , where  $\mathbf{k}^*$  is a momentum of the first particle in PRF.

### 3.2.2 Two particle wave function

Let us consider two identical particles with momenta  $\mathbf{p}_1$  and  $\mathbf{p}_2$  emitted from space points  $\mathbf{x}_1$  and  $\mathbf{x}_2$ . Those emitted particles can be treated as two incoherent waves. If the particles are identical, they are also indistinguishable, therefore one

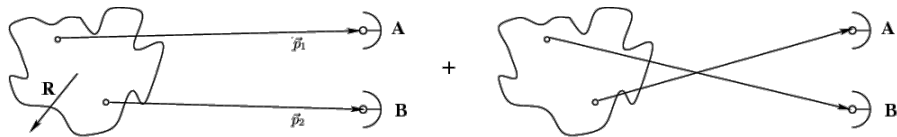


Figure 3.2: The pair wave function is a superposition of all possible states. In case of particle interferometry it includes two cases: particles with momenta  $p_1, p_2$  registered by detectors A, B and  $p_1, p_2$  registered by B, A respectively.

has also take into account the scenario, where the particle with momentum  $\mathbf{p}_1$  is emitted from  $\mathbf{x}_2$  and particle  $\mathbf{p}_2$  from  $\mathbf{x}_1$  (Fig. 3.2). In such case, the wave function describing behaviour of a pair has to contain both components [8]:

$$\Psi_{ab}(\mathbf{q}) = \frac{1}{\sqrt{2}} [\exp(-i\mathbf{p}_1\mathbf{x}_1 - i\mathbf{p}_2\mathbf{x}_2) \pm \exp(-i\mathbf{p}_2\mathbf{x}_1 - i\mathbf{p}_1\mathbf{x}_2)] . \quad (3.5)$$

A two particle wave function of identical bosons is symmetric ("+" sign in Eq. 3.5) and in case of identical fermions - antisymmetric ("-" sign). This anti-symmetrization or symmetrization implies the correlation effect coming from the Fermi-Dirac or Bose-Einstein statistics accordingly.

To provide full description of a system consisting of two charged hadrons, one has to include in the wave function besides quantum statistics also Coulomb and strong Final State Interactions. The aim of this work is an analysis of femtoscopic radii proportional to the inverse of a width of a correlation function (for detailed description see Section 3.2.4). Since we are not interested in the direct comparison of experimental correlation functions with their analytical forms, the following simplification can be made. A width of identical particles correlation function is determined by effects coming from quantum statistics, hence one can ignore influence of Final State Interactions, which in this case is small. Taking into account only quantum statistics can reduce complexity of calculations and save computation time.

705 **3.2.3 Source emission function**

706 To describe particle emitting source, one uses a single emission function [25]:

707

$$S_A(\mathbf{x}_1, \mathbf{p}_1) = \int S(\mathbf{x}_1, \mathbf{p}_1, \mathbf{x}_2, \mathbf{p}_2, \dots, \mathbf{x}_N, \mathbf{p}_N) d\mathbf{x}_2 d\mathbf{p}_2 \dots d\mathbf{x}_N d\mathbf{p}_N \quad (3.6)$$

708 and a two-particle one:

$$S_{AB}(\mathbf{x}_1, \mathbf{p}_1, \mathbf{x}_2, \mathbf{p}_2) = \int S(\mathbf{x}_1, \mathbf{p}_1, \mathbf{x}_2, \mathbf{p}_2, \dots, \mathbf{x}_N, \mathbf{p}_N) d\mathbf{x}_3 d\mathbf{p}_3 \dots d\mathbf{x}_N d\mathbf{p}_N . \quad (3.7)$$

709 Emission function  $S(\cdot)$  can be interpreted as a probability to emit a particle, or  
 710 a pair of particles from a given space-time point with a given momentum. In  
 711 principle, the source emission function should encode all physics aspects of the  
 712 particle emission process i.e. the symmetrization for bosons and fermions, as  
 713 well as the two-body and many body Final State Interactions. Instead of this,  
 714 one assume that each particle's emission process is independent - the interac-  
 715 tion between final-state particles after their creation is independent from their  
 716 emission process. The assumption of this independence allows to construct two-  
 717 particle emission function from single particle emission functions via a convolu-  
 718 tion [25]:

$$S(\mathbf{k}^*, \mathbf{r}^*) = \int S_A(\mathbf{p}_1, \mathbf{x}_1) S_B(\mathbf{p}_2, \mathbf{x}_2) \delta \left[ \mathbf{k}^* - \frac{\mathbf{p}_1 + \mathbf{p}_2}{2} \right] \delta [\mathbf{r}^* - (\mathbf{x}_1 + \mathbf{x}_2)] \times d^4 \mathbf{x}_1 d^4 \mathbf{x}_2 d^4 \mathbf{x}_1 d^3 \mathbf{p}_1 d^3 \mathbf{p}_2 \quad (3.8)$$

719 In case of identical particles, ( $S_A = S_B$ ) several simplifications can be made. A  
 720 convolution of the two identical Gaussian distributions is also a Gaussian distri-  
 721 bution with  $\sigma$  multiplied by  $\sqrt{2}$ . Femtoscopy can give information only about  
 722 two-particle emission function, but when considering Gaussian distribution as  
 723 a source function in Eq. 3.8, one can obtain a  $\sigma$  of a single emission function  
 724 from a two-particle emission function. The Eq. 3.8 is not reversible - an inform-  
 725 ation about  $S_A(\cdot)$  cannot be derived from  $S_{AB}(\cdot)$ . An exception from this rule  
 726 is a Gaussian source function, hence it is often used in femtoscopic calculations.  
 727 Considering pairs of identical particles, an emission function is assumed to be  
 728 described by the following equation in the Pair Rest Frame [25]:

$$S_{1D}^{PRF}(\mathbf{r}^*) = \exp \left( -\frac{r_{out}^{*2} + r_{side}^{*2} + r_{long}^{*2}}{4R_{inv}^2} \right) . \quad (3.9)$$

To change from the three-dimensional variables to the one-dimensional variable  
 one requires introduction of the proper Jacobian  $r^{*2}$ .

$$S_{1D}^{PRF}(r^*) = r^{*2} \exp \left( -\frac{r^{*2}}{4R_{inv}^2} \right) . \quad (3.10)$$

729 The “4” in the denominator before the “standard deviation”  $R_{inv}$  in the Gaussian  
 730 distribution comes from the convolution of the two Gaussian distributions,  
 731 which multiplies the  $R_{inv}$  by a factor of  $\sqrt{2}$ .

A more complex form of emission function was used by all RHIC and SPS experiments in identical pion femtoscopy:

$$S_{3D}^{LCMS}(\mathbf{r}) = \exp \left( -\frac{r_{out}^2}{4R_{out}^2} - \frac{r_{side}^2}{4R_{side}^2} - \frac{r_{long}^2}{4R_{long}^2} \right). \quad (3.11)$$

732 The main difference of this source function is that it has three different and inde-  
 733 pendent widths  $R_{out}$ ,  $R_{side}$ ,  $R_{long}$  and they are defined in the LCMS, not in PRF.  
 734 Unlike in PRF, in LCMS an equal-time approximation is not used. For identical  
 735 particles this is not a problem - only Coulomb interaction inside a wave function  
 736 depends on  $\Delta t$ .

### 737 Relationship between one-dimensional and three-dimensional source sizes

738 Up to now, most of femtoscopic measurements were limited only to averaged  
 739 source size  $R_{av}^L$  (the letter “L” in superscript stands for LCMS):

$$S_{1D}^{LCMS}(\mathbf{r}) = \exp \left( -\frac{r_{out}^2 + r_{side}^2 + r_{long}^2}{2R_{av}^L} \right). \quad (3.12)$$

740 The relationship between between  $S_{1D}^{LCMS}(\cdot)$  and  $S_{3D}^{LCMS}(\cdot)$  is given by:

$$S_{3D}^{LCMS}(r) = \int \exp \left( -\frac{r_{out}^2}{2R_{out}^L} - \frac{r_{side}^2}{2R_{side}^L} - \frac{r_{long}^2}{2R_{long}^L} \right) \times \delta \left( r - \sqrt{r_{out}^2 + r_{side}^2 + r_{long}^2} \right) dr_{out} dr_{side} dr_{long}. \quad (3.13)$$

741 The one-dimensional source size corresponding to the three-dimensional one can  
 742 be approximated by the following form:

$$S_{1D}^{LCMS}(r) = r^2 \exp \left( -\frac{r^2}{2R_{av}^L} \right). \quad (3.14)$$

743 The equation above assumes that  $R_{out}^L = R_{side}^L = R_{long}^L$  hence  $R_{av}^L = R_{out}^L$ . If this  
 744 condition is not satisfied, one can not give explicit mathematical relation between  
 745 one-dimensional and three-dimensional source sizes. However, for realistic val-  
 746 ues of  $R$  (i.e. for similar values of  $R_{out}$ ,  $R_{side}$ ,  $R_{long}$ ), the  $S_{3D}^{LCMS}$  from Eq. 3.13 is  
 747 not very different from Gaussian distribution and can be well approximated by  
 748 Eq. 3.13.

749 A deformation of an averaged source function in case of big differences in  
 750  $R_{out}$ ,  $R_{side}$ ,  $R_{long}$  is presented in the Fig. 3.3. A three-dimensional Gaussian dis-  
 751 tribution with varying widths was averaged into one-dimensional function using

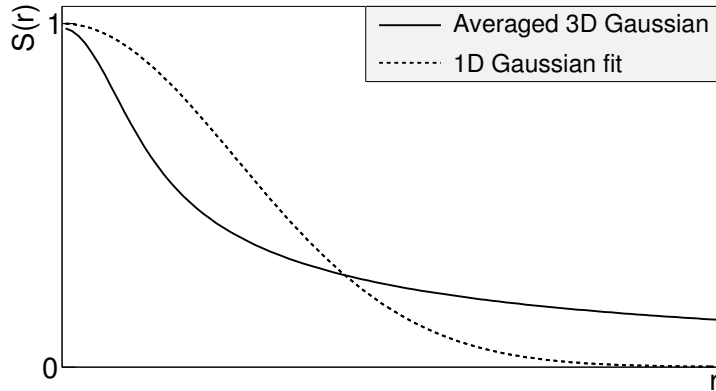


Figure 3.3: An averaged three-dimensional Gaussian source function with different widths was averaged into one-dimensional function. To illustrate deformations, one-dimensional Gaussian distribution was fitted.

the Eq. 3.13. Afterwards, an one-dimensional Gaussian distribution was fitted.  
One can notice a heavy tail of an averaged distribution in long  $r$  region, which  
makes an approximation using one-dimensional distribution in this case quite  
inaccurate.

Using Eq. 3.13 and Eq. 3.14 one can obtain a relation between one-dimensional width and the three-dimensional ones. Through numerical calculations one can find the following approximate relation [25]:

$$R_{av}^L = \sqrt{\left(R_{out}^{L^2} + R_{side}^{L^2} + R_{long}^{L^2}\right)/3}. \quad (3.15)$$

This equation does not depend on the pair velocity, hence it is valid in the LCMS and PRF.

### 3.2.4 Analytical form of a correlation function

The fundamental object in a particle interferometry is a correlation function. The correlation function is defined as:

$$C(\mathbf{p}_a, \mathbf{p}_b) = \frac{P_2(\mathbf{p}_a, \mathbf{p}_b)}{P_1(\mathbf{p}_a)P_1(\mathbf{p}_b)}, \quad (3.16)$$

where  $P_2$  is a conditional probability to observe a particle with momentum  $\mathbf{p}_b$  if particle with momentum  $\mathbf{p}_a$  was also observed. A  $P_1$  is a probability to observe a particle with a given momentum. The relationship between source emission function, pair wave function and the correlation function is described by the following equation:

$$C(\mathbf{p}_1, \mathbf{p}_2) = \int S_{AB}(\mathbf{p}_1, \mathbf{x}_1, \mathbf{p}_2, \mathbf{x}_2) |\Psi_{AB}|^2 d^4\mathbf{x}_1 d^4\mathbf{x}_2 \quad (3.17)$$

Substituting the one-dimensional emission function (Eq. 3.10) into the integral above yields the following form of correlation function in PRF:

$$C(q) = 1 + \lambda \exp(-R_{inv}^2 q^2) \quad (3.18)$$

where  $q$  is a momentum difference between two particles. When using the three-dimensional emission function (Eq. 3.11) one gets the following correlation function defined in the LCMS:

$$C(\mathbf{q}) = 1 + \lambda \exp(-R_{out}^2 q_{out}^2 - R_{side}^2 q_{side}^2 - R_{long}^2 q_{long}^2) \quad (3.19)$$

where  $q_{out}$ ,  $q_{side}$ ,  $q_{long}$  are  $\mathbf{q}$  components in the outward, sideward and longitudinal direction. The  $\lambda$  parameter in the equations above determines correlation strength. The lambda parameter has values in the range  $\lambda \in [-0.5, 1]$  and it depends on a pair type. In case of pairs of identical bosons (like  $\pi\pi$  or  $KK$ ) the lambda parameter  $\lambda \rightarrow 1$ . For identical fermions (e.g.  $p-p$ )  $\lambda \rightarrow -0.5$ . Values of  $\lambda$  observed experimentally are lower than 1 (for bosons) and greater than -0.5 (for fermions). There are few explanations to this effect: detector efficiencies, inclusion of misidentified particles in a used sample or inclusion of non-correlated pairs (when one or both particles come from e.g. long-lived resonance). The analysis carried out in this work uses data from a model, therefore the detector efficiency and particle purity is not taken into account [25].

### 3.2.5 Spherical harmonics decomposition of a correlation function

Results coming from an analysis using three-dimensional correlation function in Cartesian coordinates are quite difficult to visualize. To do that, one usually performs a projection into one dimension in outward, sideward and longitudinal directions. One may loose important information about a correlation function in this procedure, because it gives only a limited view of the full three-dimensional structure. Recently, a more advanced way of presenting correlation function - a spherical harmonics decomposition, was proposed. The three-dimensional correlation function is decomposed into an infinite set of components in a form of one-dimensional histograms  $C_l^m(q)$ . In this form, a correlation function is defined as a sum of a series [26]:

$$C(\mathbf{q}) = \sum_{l,m} C_l^m(q) Y_l^m(\theta, \phi), \quad (3.20)$$

where  $Y_l^m(\theta, \phi)$  is a spherical harmonic function. Spherical harmonics are an orthogonal set of solutions to the Laplace's equation in spherical coordinates. Hence, in this approach, a correlation function is defined as a function of  $q$ ,  $\theta$  and  $\phi$ . To obtain  $C_l^m$  coefficients in the series, one has to calculate the following integral:

$$C_l^m(q) = \int_{\Omega} C(q, \theta, \phi) Y_l^{m*}(\theta, \phi) d\Omega, \quad (3.21)$$

793 where  $\Omega$  is a full solid angle.

Spherical harmonics representation has several important advantages. The main one is that it requires less statistics than traditional analysis performed in Cartesian coordinates. Another one is that it encodes full three-dimensional information in a set of one-dimensional plots. In principle it does not have to be an advantage, because full description of a correlation function requires infinite number of  $l, m$  components. But it so happens that the intrinsic symmetries of a pair distribution in a femtoscopic analysis result in most of the components to vanish. For the identical particles correlation functions, all coefficients with odd values of  $l$  and  $m$  disappear. It has also been shown, that the most significant portion of femtoscopic data is stored in the components with the lowest  $l$  values. It is expected that, the main femtoscopic information is contained in the following components [25]:

$$C_0^0 \rightarrow R_{LCMS}, \quad (3.22)$$

$$\Re C_2^0 \rightarrow \frac{R_T}{R_{long}}, \quad (3.23)$$

$$\Re C_2^2 \rightarrow \frac{R_{out}}{R_{side}}, \quad (3.24)$$

794 where  $R_{LCMS} = \sqrt{(R_{out}^2 + R_{side}^2 + R_{long}^2)/3}$  and  $R_T = \sqrt{(R_{out}^2 + R_{side}^2)/2}$ .

795 The  $C_0^0$  is sensitive to the overall size of a correlation function. The  $\Re C_2^0$  carries  
 796 the information about the ratio of the transverse to the longitudinal radii, due  
 797 to its  $\cos^2(\theta)$  weighting in  $Y_2^0$ . The component  $\Re C_2^2$  with its  $\cos^2(\phi)$  weighting  
 798 encodes the ratio between outward and sideward radii. Thus, the spherical har-  
 799 monics method allows to obtain and analyze full three-dimensional femtoscopic  
 800 information from a correlation function [25].

### 801 3.3 Experimental approach

802 The correlation function is defined as a probability to observe two particles  
 803 together divided by the product of probabilities to observe each of them sepa-  
 804 rately (Eq. 3.16). Experimentally this is achieved by dividing two distributions  
 805 of relative momentum of pairs of particles coming from the same event and the  
 806 equivalent distribution of pairs where each particle is taken from different colli-  
 807 sions. In this way, one obtains not only femtoscopic information but also all other  
 808 event-wide correlations. This method is useful for experimentalists to estimate  
 809 the magnitude of non-femtoscopic effects. There exists also a different approach,  
 810 where two particles in pairs in the second distribution are also taken from the  
 811 same event. The second method gives only information about physical effects  
 812 accessible via femtoscopy. The aim of this work is a study of effects coming from  
 813 two particle interferometry, hence the latter method was used.

814 In order to calculate experimental correlation function, one uses the follow-  
 815 ing approach. One has to construct two histograms: the *numerator*  $N$  and the

816 denominator  $D$  with the particle pairs momenta, where particles are coming from  
 817 the same event. Those histograms can be one-dimensional (as a function of  $|\mathbf{q}|$ ),  
 818 three dimensional (a function of three components of  $\mathbf{q}$  in LCMS) or a set of one-  
 819 dimensional histogram representing components of the spherical harmonic de-  
 820 composition of the distribution. The second histogram,  $D$  is filled for each pair  
 821 with the weight 1.0 at a corresponding relative momentum  $\mathbf{q} = 2\mathbf{k}^*$ . The first one,  
 822  $N$  is filled with the same procedure, but the weight is calculated as  $|\Psi_{ab}(\mathbf{r}^*, \mathbf{k}^*)|^2$ .  
 823 A division  $N/D$  gives the correlation function  $C$ . This procedure can be simply  
 824 written as [25]:

$$C(\mathbf{k}^*) = \frac{N}{D} = \frac{\sum_{n_i \in D} \delta(\mathbf{k}_i^* - \mathbf{k}^*) |\Psi_{ab}(\mathbf{r}_i^*, \mathbf{k}_i^*)|^2}{\sum_{n_i \in D} \delta(\mathbf{k}_i^* - \mathbf{k}^*)} . \quad (3.25)$$

The  $D$  histogram represents the set of all particle pairs used in calculations.  
 The  $n_i$  is a pair with the its relative momentum  $\mathbf{k}_i^*$  and relative separation  $\mathbf{r}_i^*$ .  
 Mathematically, the procedure of calculating the Eq. 3.25 is equivalent to a  
 calculation of an integral in Eq. 3.17 through a Monte-Carlo method. The wave  
 function used in Eq. 3.25 has one of the following forms:

$$|\Psi_{\pi\pi}(\mathbf{r}^*, \mathbf{k}^*)|^2 = |\Psi_{KK}(\mathbf{r}^*, \mathbf{k}^*)|^2 = 1 + \cos(2\mathbf{k}^* \mathbf{r}^*) , \quad (3.26)$$

$$|\Psi_{pp}(\mathbf{r}^*, \mathbf{k}^*)|^2 = 1 - \frac{1}{2} \cos(2\mathbf{k}^* \mathbf{r}^*) . \quad (3.27)$$

825 The first one is used in case of bosons, and the latter one is for identical fermions.  
 826 A wave function for pair of spin-1/2 fermions (Eq. 3.27) is a superposition of two  
 827 possible states: singlet state (with spin equal to 0 and one eigenstate) and triplet  
 828 state (with spin equal to 1 and three possible eigenstates). For a singlet state, a  
 829 wave function is symmetric, and for triplet state, it is antisymmetric. In other  
 830 words the  $|\Psi_{pp}|^2$  encodes correlation coming from Bose-Einstein statistics (with  
 831 weight 1/4) and anti-correlation from Fermi-Dirac distribution (with weight 3/4).

### 832 3.4 Scaling of femtoscopy radii

833 A particle interferometry formalism presented in the previous sections as-  
 834 sumes that particle emitting source is static. This is not the case in heavy ion  
 835 collisions at LHC. An existence of transverse radial and elliptic flow suggest that  
 836 created system is dynamic. To address this issue, a concept of *lengths of homogen-*  
 837 *eity* was introduced. It is defined as:

$$\frac{|f(p, x + \lambda) - f(p, x)|}{f(p, x)} = 1 , \quad (3.28)$$

838 where  $\lambda$  is the homogeneity length. It can be interpreted as the distance at which  
 839 relative change of the source Wigner function  $f$  becomes large. One can measure

the lengths of homogeneity of a system using femtoscopic radii. This concept can be intuitively explained on a basis of hydrodynamic models. Each source element is emitting particles with a velocity which is a combination of two components: a fluid cell velocity  $\beta_f$  (which is taken from the flow field  $u_\mu(x^\mu)$ ) and thermal velocity  $\beta_{th}$  (which has random direction). These particles can combine into pairs of small relative momenta and become correlated. If two particles are emitted far ( $|x_a - x_b| > \lambda$ ) away from each other, the flow field  $u_\mu$  in their point of emission might be very different and it will be impossible for them to have sufficiently small relative momenta to be in the region of interference effect. This effect is presented in Fig. 3.4. An increase of a correlation is visible for pairs with low relative momenta [8].

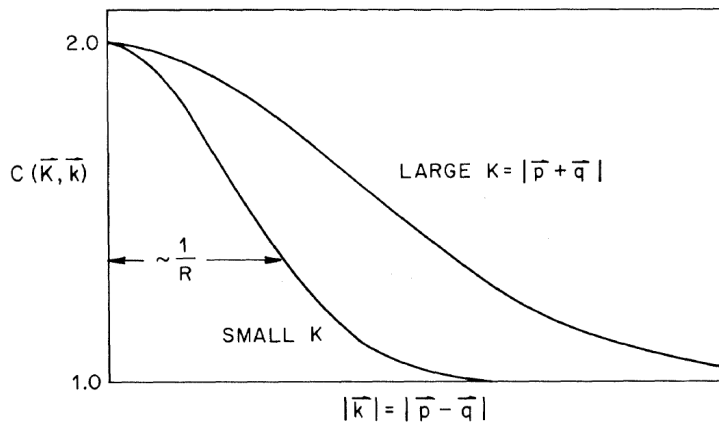


Figure 3.4: Correlation function width dependence on total pair momentum. Pion pairs with a large total momentum have a wider correlation (smaller apparent source) [27].

850

### 851 3.4.1 Scaling in LCMS

Hydrodynamic calculations performed in LCMS show that femtoscopic radii in outward, sideward, and longitudinal direction show dependence on transverse mass  $m_T = \sqrt{k_T^2 + m^2}$ , where  $m$  is a mass of a particle [28]. Moreover, experimental results show that this scaling is observed for  $R_{LCMS}$  radii also. This dependence can be expressed as follows:

$$R_i = \alpha m_T^{-\beta} \quad (3.29)$$

852 where  $i$  subscript indicates that this equation applies to  $R_{out}$ ,  $R_{side}$  and  $R_{long}$   
 853 radii. The  $\beta$  exponent is approximately equal 0.5. In case of strong transversal  
 854 expansion of the emitting source, the decrease of longitudinal interferometry ra-  
 855 dius can be more quick than  $m_T^{-0.5}$ , hence one can expect for longitudinal radii  
 856 greater values of  $\beta > 0.5$  [28].

857 **3.4.2 Scaling in PRF**

858 In the collisions at the LHC energies, pions are most abundant particles and  
 859 their multiplicities are large enough to enable three-dimensional analysis. How-  
 860 ever, for heavier particles, such as kaons and protons statistical limitations arise.  
 861 Hence it is often possible to only measure one-dimensional radius  $R_{inv}$  for those  
 862 particles. The  $R_{inv}$  is then calculated in the PRF. The transition from LCMS to  
 863 PRF is a Lorentz boost in the direction of pair transverse momentum with velo-  
 864 city  $\beta_T = p_T/m_T$ . Hence only  $R_{out}$  radius changes:

$$R_{out}^* = \gamma_T R_{out}. \quad (3.30)$$

865 The one-dimensional  $R_{inv}$  radius is direction-averaged source size in PRF. One  
 866 can notice, that such power-law scaling of  $R_{inv}$  described by Eq. 3.29 is not  
 867 observed. To recover such scaling in PRF one has to take into consideration two  
 868 effects when transforming variables from LCMS to PRF: overall radius growths  
 869 and source distribution becomes non-Gaussian, while developing long-range  
 870 tails (see Fig. 3.3 for an example). The interplay of these two effects can be  
 871 accounted with an approximate formula:

$$R_{inv} = \sqrt{(R_{out}^2 \sqrt{\gamma_T} + R_{side}^2 + R_{long}^2)/3}. \quad (3.31)$$

Assuming that all radii are equal  $R_{out} = R_{side} = R_{long}$  this formula can be sim-  
 plified:

$$R_{LCMS} \approx R_{inv} \times [(\sqrt{\gamma_T} + 2)/3]^{-1/2}. \quad (3.32)$$

872 This approximate formula allows to restore power-law behaviour of the scaled  
 873 radii not only when the radii are equal, but also when their differences are small  
 874 (for explanation see the last part of the section 3.2.3).

875 This method of recovering scaling in PRF can be used as a tool for the search  
 876 of hydrodynamic collectivity between pions, kaons and protons in heavy ion col-  
 877 lisions with the measurement of one-dimensional radius in PRF.

878    **Chapter 4**

879    **Results**

880    For the purposes of the femtoscopic analysis in this thesis, the THERMINATOR  
881    model was used to generate large number of events for eight different sets of  
882    initial conditions corresponding the following centrality ranges: 0-5%, 0-10%, 10-  
883    20%, 20-30%, 30-40%, 40-50%, 50-60% and 60-70% for the Pb-Pb collisions at the  
884    centre of mass energy  $\sqrt{s_{NN}} = 2.76 \text{ TeV}$ .

885    **4.1 Identical particles correlations**

886    The correlation functions (three-dimensional and one-dimensional) were cal-  
887    culated separately for the following different pairs of identical particles:  $\pi$ - $\pi$ ,  $K$ -  
888     $K$  and  $p$ - $p$  for nine  $k_T$  bins (in GeV/c): 0.1-0.2, 0.2-0.3, 0.3-0.4, 0.4-0.5, 0.6-0.7,  
889    0.7-0.8, 0.8-1.0 and 1.0-1.2. In case of kaons,  $k_T$  ranges start from 0.3 and for pi-  
890    ons from 0.4 and for both of them the maximum value is 1.0. The  $k_T$  ranges for  
891    the heavier particles were limited to maintain sufficient multiplicity to perform  
892    reliable calculations.

893    **4.1.1 Spherical harmonics components**

894    The three-dimensional correlation function as a function of relative  
895    momentum  $q_{LCMS}$  was calculated in a form of components of spherical  
896    harmonics series accordingly to the Eq. 3.21. In the femtoscopic analysis of  
897    identical particles, the most important information is stored in the  $\Re C_0^0$ ,  $\Re C_2^0$   
898    and  $\Re C_2^2$ , hence only those components were analyzed. Correlation functions  
899    obtained in this procedure were calculated for the different centrality bins for the  
900    pairs of pions, kaons and protons. They are presented in the Fig. 4.1, 4.2 and 4.3.

901    Coefficients for pairs of identical bosons (pions and kaons) are shown in the  
902    Fig. 4.1 and 4.2. The wave function symmetrization (Bose-Einstein statistics)  
903    causes the increase of a correlation in the low relative momenta regime ( $q_{LCMS} <$   
904    0.06 GeV/c or even  $q_{LCMS} < 0.12 \text{ GeV/c}$  for more peripheral collisions). It is  
905    clearly visible in the  $\Re C_0^0$  component. The  $\Re C_0^0$  resembles one-dimensional cor-

relation function and in fact it encodes information about overall source radius. The second coefficient  $\Re C_2^0$  differs from zero (is negative), which yields the information about the ratio  $R_T/R_{long}$ . The  $\Re C_2^2$  stores the  $R_{out}/R_{side}$  ratio and one can notice that is non-vanishing (is also negative).

The correlation function for a pair of identical fermions is presented in the Fig. 4.3. An influence of wave function anti-symmetrization (Fermi-Dirac statistics) has its effect in the decrease of a correlation down to 0.5 at low relative momentum ( $q_{LCMS} < 0.1 \text{ GeV/c}$  or  $q_{LCMS} < 0.15 \text{ GeV/c}$  for more peripheral collisions), which can be observed in  $\Re C_0^0$ . The  $\Re C_2^0$  and  $\Re C_2^2$  coefficients differ from zero and are becoming positive.

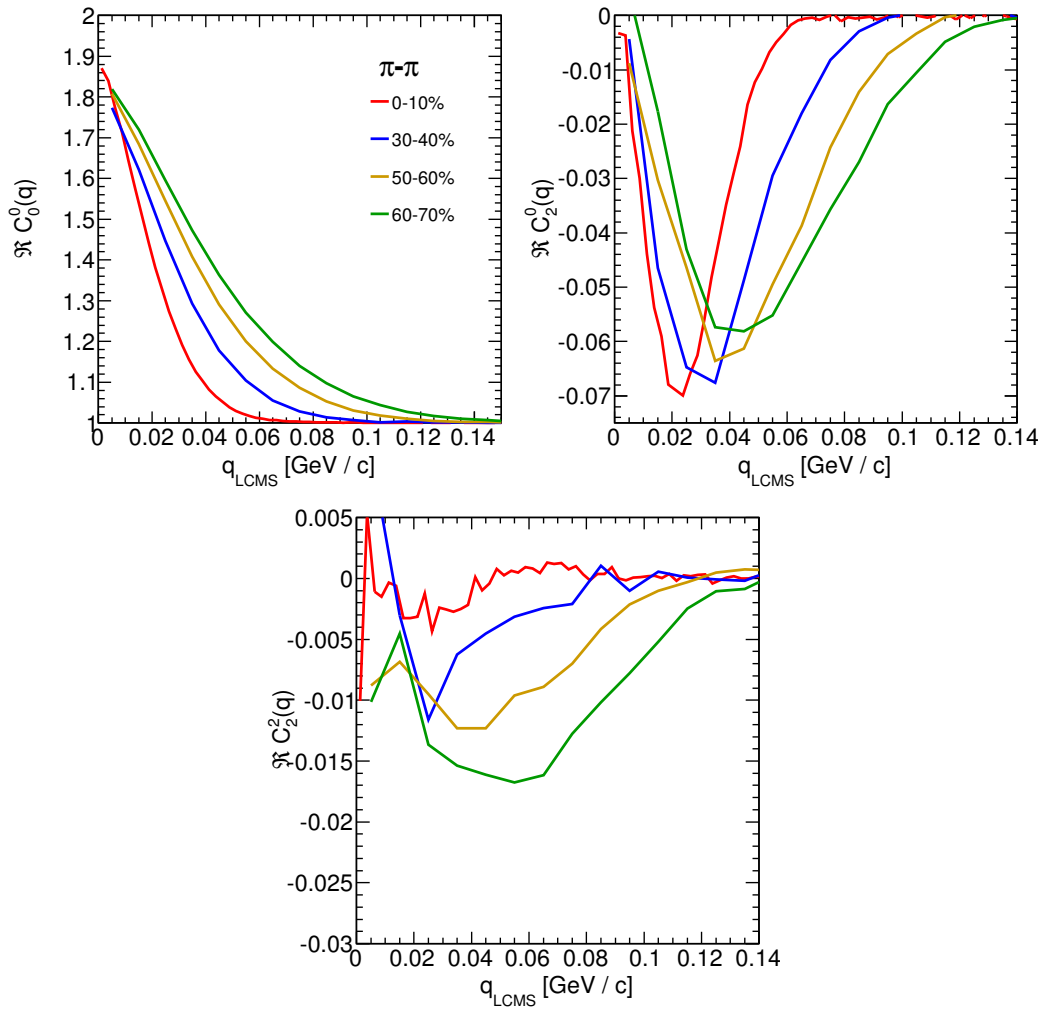


Figure 4.1: Spherical harmonics coefficients of the two-pion correlation function. From the top left:  $\Re C_0^0$ ,  $\Re C_2^0$  and  $\Re C_2^2$ . Only few centrality bins are presented for increased readability.

916      The common effect of the spherical harmonics form of a correlation function  
 917      is the “mirroring” of the shape of the  $\Re C_0^0$  coefficient - when correlation func-  
 918      tion increases at low  $q_{LCMS}$ , the  $\Re C_2^0$  and  $\Re C_2^2$  are becoming negative and vice  
 919      versa. This is quite different behaviour than in the case of correlations of non-  
 920      identical particles, where the  $\Re C_2^0$  still behaves in the same manner, but  $\Re C_2^2$  has  
 921      the opposite sign to the  $\Re C_2^0$  [25].

922      In all cases, the correlation function gets wider with the peripherality of a  
 923      collision i.e. the correlation function for most central collisions (0-10%) is much  
 924      narrower than for the most peripheral ones (60-70%). This phenomena in clearly

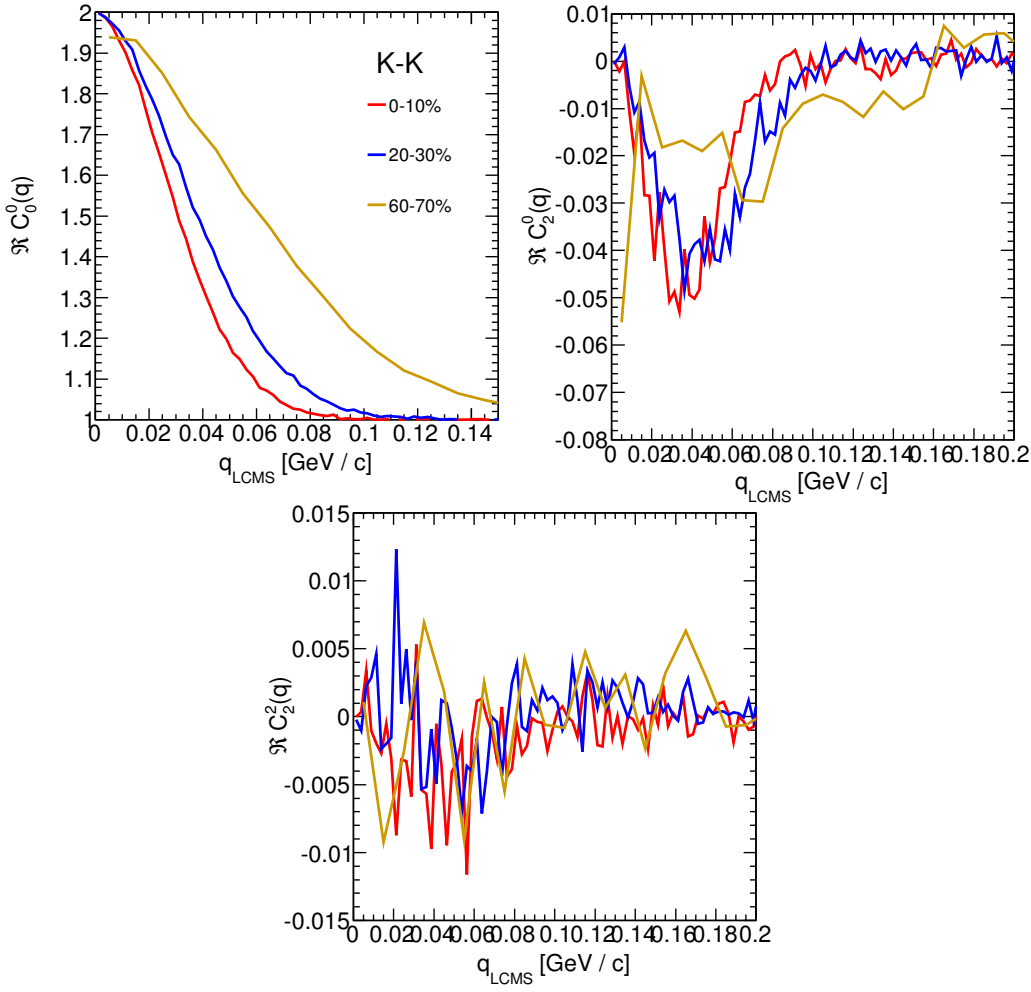


Figure 4.2: Spherical harmonics coefficients of the two-kaon correlation function. From the top left:  $\Re C_0^0$ ,  $\Re C_2^0$  and  $\Re C_2^2$ . Only few centrality bins are presented for increased readability. The  $\Re C_2^2$  is noisy, but one can still notice that it differs from zero and is becoming negative.

visible the  $\Re C_0^0$  coefficients. Other components are also affected by this effect, this is especially noticeable in the case of kaons and pions. For the protons, the results are noisy, hence this effect is not clearly distinguishable.

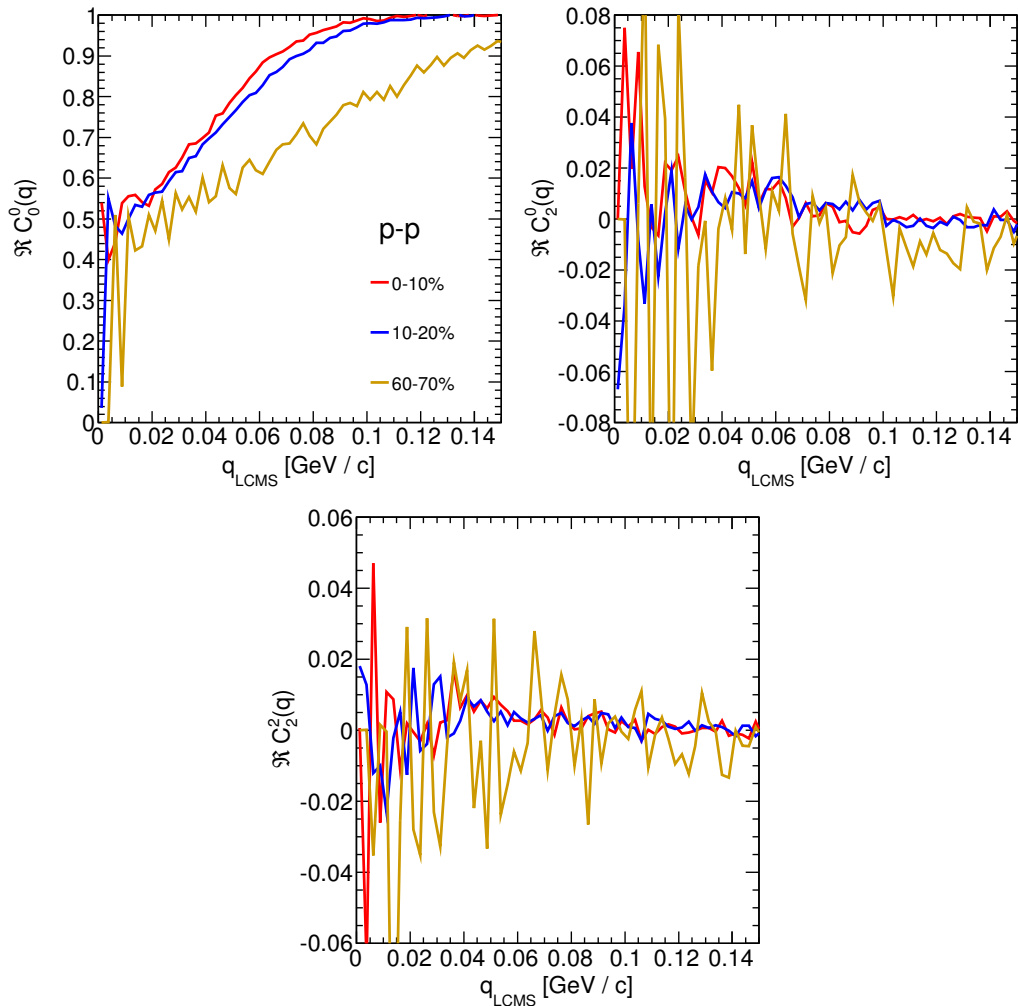


Figure 4.3: Spherical harmonics coefficients of the two-proton correlation function. From the top left:  $\Re C_0^0$ ,  $\Re C_2^0$  and  $\Re C_2^2$ . Only few centrality bins are presented for increased readability. The  $\Re C_2^0$  and  $\Re C_2^2$  are noisy, but one can still notice, that they differ from zero and are becoming positive.

928 **4.1.2 Centrality dependence of a correlation function**

929     The centrality dependence of a correlation function is especially visible in  
 930     one-dimensional correlation functions. This effect is presented in the Fig. 4.4 -  
 931     the correlation functions for pions, kaons and protons are plotted for the same  
 932      $k_T$  range but different centrality bins. One can notice that the width of a func-  
 933     tion is smaller in the case of most central collisions. Hence, the femtoscopic radii  
 934     (proportional to the inverse of width) are increasing with the centrality. An ex-  
 935     planation for this growth is that in the most central collisions, a size of a created  
 system is larger than for the peripheral ones.

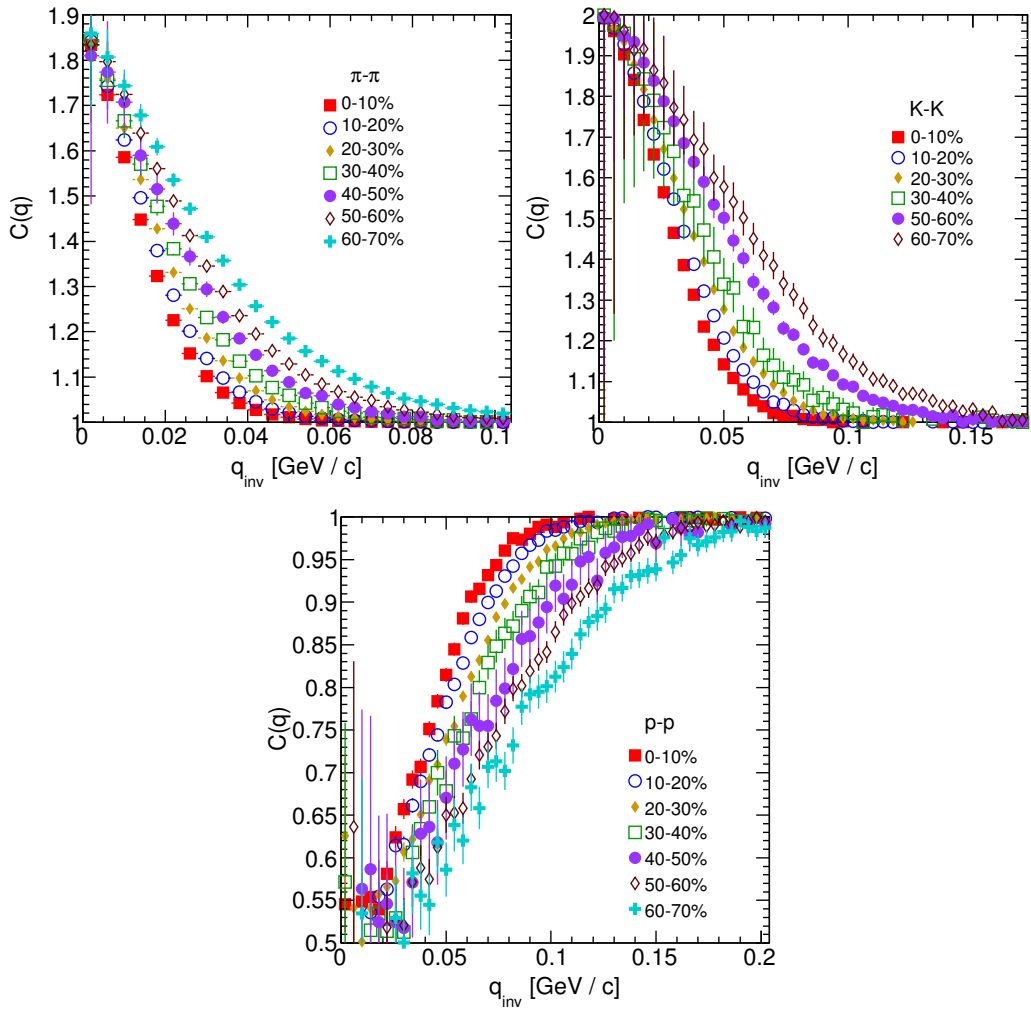


Figure 4.4: One-dimensional correlation function for pions (top left), kaons (top right) and protons (bottom) for different centralities.

937 **4.1.3  $k_T$  dependence of a correlation function**

938 In the Fig. 4.5 there are presented one-dimensional correlation functions for  
 939 pions, kaons and protons for the same centrality bin, but different  $k_T$  ranges. One  
 940 can observe in all cases of the particle types, appearance of the same trend: with  
 941 the increase of the total transverse momentum of a pair, the width of a correlation  
 942 function increases and the femtoscopic radius decreases. The plots in the Fig. 4.5  
 943 were zoomed in to show the influence of  $k_T$ .

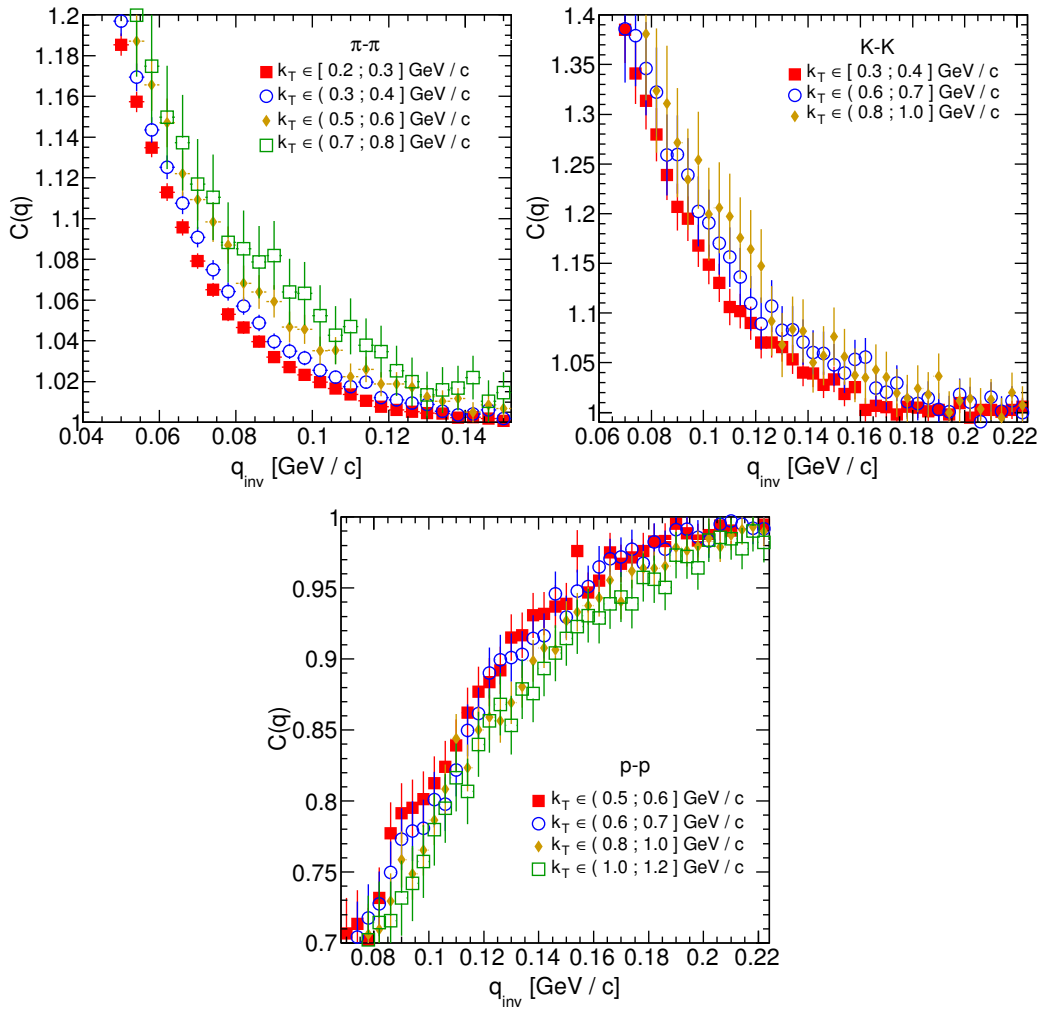


Figure 4.5: One-dimensional correlation functions for pions, kaons and protons, for the same centrality bin and different  $k_T$  ranges. The plot was zoomed in to the region which illustrates the  $k_T$  dependence in the best way. Only few of the calculated ranges are presented for better readability.

## 4.2 Results of the fitting procedure

In order to perform a quantitative analysis of a wide range of correlation functions, the theoretical formulas were fitted to the calculated experimental-like data. In this procedure, the femtoscopic radii for the three-dimensional as well as one-dimensional correlation functions were extracted. The main goal of this analysis is a verification of a common transverse mass scaling for different particles types. Obtained radii are plotted as a function of a transverse mass  $m_T = \sqrt{k_T^2 + m^2}$ . To test the scaling, the following power-law was fitted to the particular radii afterwards:

$$R_x = \alpha m_T^{-\beta}, \quad (4.1)$$

where the  $\alpha$  and  $\beta$  are free parameters.

### 4.2.1 The three-dimensional femtoscopic radii scaling

In the Fig. 4.6 there are presented femtoscopic radii in the outward, sideward and longitudinal directions for the analysis of two-pion correlation functions in

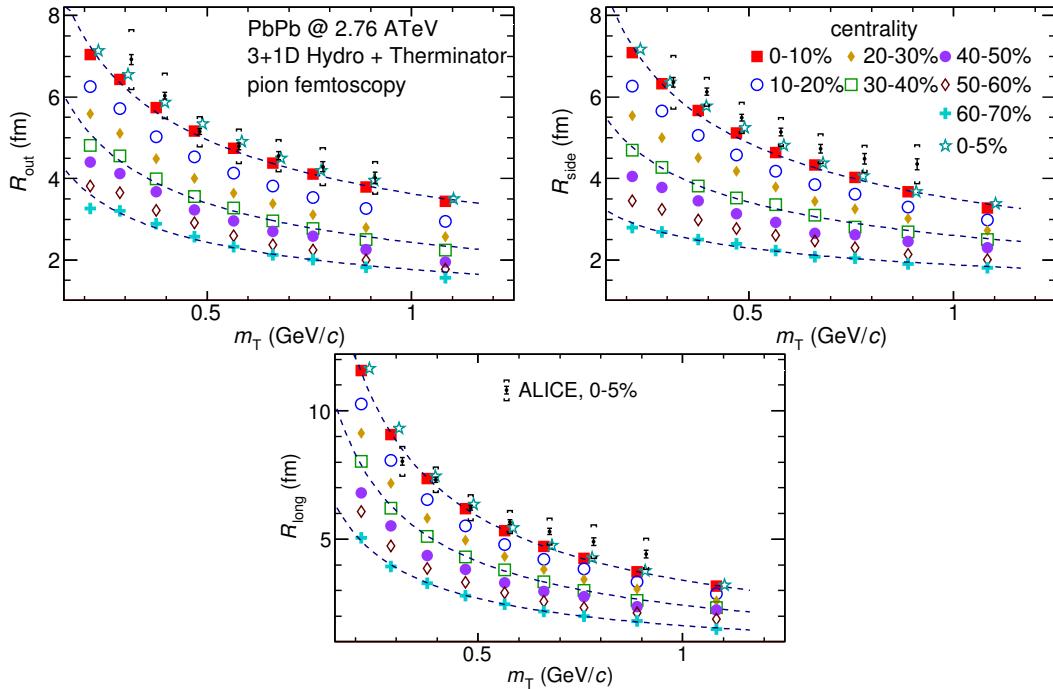


Figure 4.6: Femtoscopic radii in LCMS coming from two-pion correlation functions for all centrality bins as a function of  $m_T$ . The dashed lines are power-law fits. The most central collisions (0-5%) are compared to the results from ALICE [29]. The two datasets are shifted to the right for visibility [30].

the LCMS. The dashed lines are fits of the power law to the data. One can notice, that the power law describes well data points with a 5% accuracy. The  $\beta$  fit parameter for the outward direction is in the order of 0.45. For the sideward direction, this parameter has the similar value, but it is lower for the most peripheral collisions. In case of the longitudinal direction, the  $\beta$  has greater value, up to 0.75. In the Fig. 4.6 there are also compared results for the top 5% central collisions (star-shaped markers) with experimental data from ALICE [29]. The experimental results are consistent with the ones coming from the model predictions.

The Fig. 4.7 presents femtoscopic radii coming from the kaon calculations. The  $R_{out}$ ,  $R_{side}$  and  $R_{long}$  fall also with the power-law within the 5% accuracy. The  $\beta$  parameter was larger in case of kaons: 0.59 in outward direction, 0.54 in the sideward and 0.86 for longitudinal.

The results for two-proton analysis are shown in the Fig. 4.8. The Eq. 4.1 was fitted to the data and tells that the protons also follow the  $m_T$  scaling within 5% range. The  $\beta$  parameter values were even bigger for the outward ( 0.58 ), sideward ( 0.61 ) and longitudinal ( 1.09 ) directions than for the other particle types.

The Fig. 4.9 presents results for the pions, kaons and protons together as a function of  $m_T$ . Considering differences in the  $\beta$  value for the fits for differ-

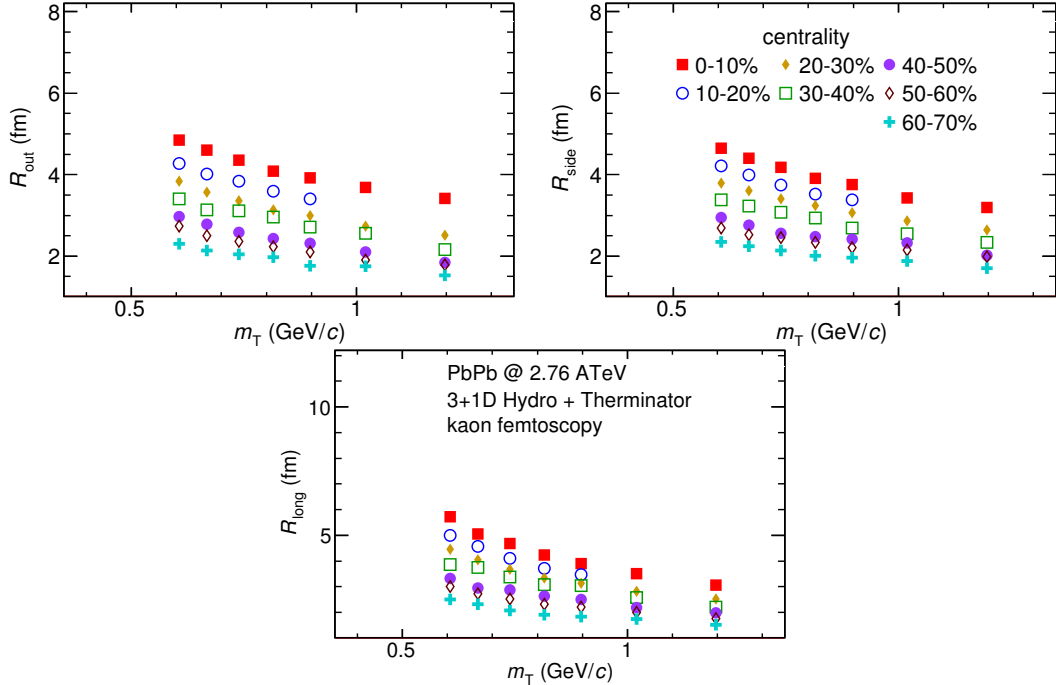


Figure 4.7: Femtoscopic radii extracted from two-kaon correlation functions for different centrality bins as a function of  $m_T$ . [30].

977 ent particles, one can suspect that there is no common scaling between different  
 978 kinds of particles. However, when all of the results shown on the same plot, they  
 979 are aligning on the common curve and the scaling is well preserved. The scaling  
 980 accuracy is 3%, 5% and 4% for the 0-10%, 20-30% and 60-70% for the outward  
 981 direction. For the sideward radii the scaling is better, with average deviations  
 982 2%, 2% and 3% respectively. In case of longitudinal direction the accuracy is 6%,  
 983 5% and 3% for the three centralities. The  $\beta$  parameter for the outward direction  
 984 is close to the 0.42 in all cases. For the sideward direction it varies from 0.28 to  
 985 0.47 and is bigger for more central collisions. Regarding longitudinal radii, the  
 986 exponent is bigger than the other two:  $\beta \in [0.62; 0.72]$ . Considering all results,  
 987 the plotted radii are following the common power-law scaling within the 5% ac-  
 988 curacy for all directions, centralities and particle types.

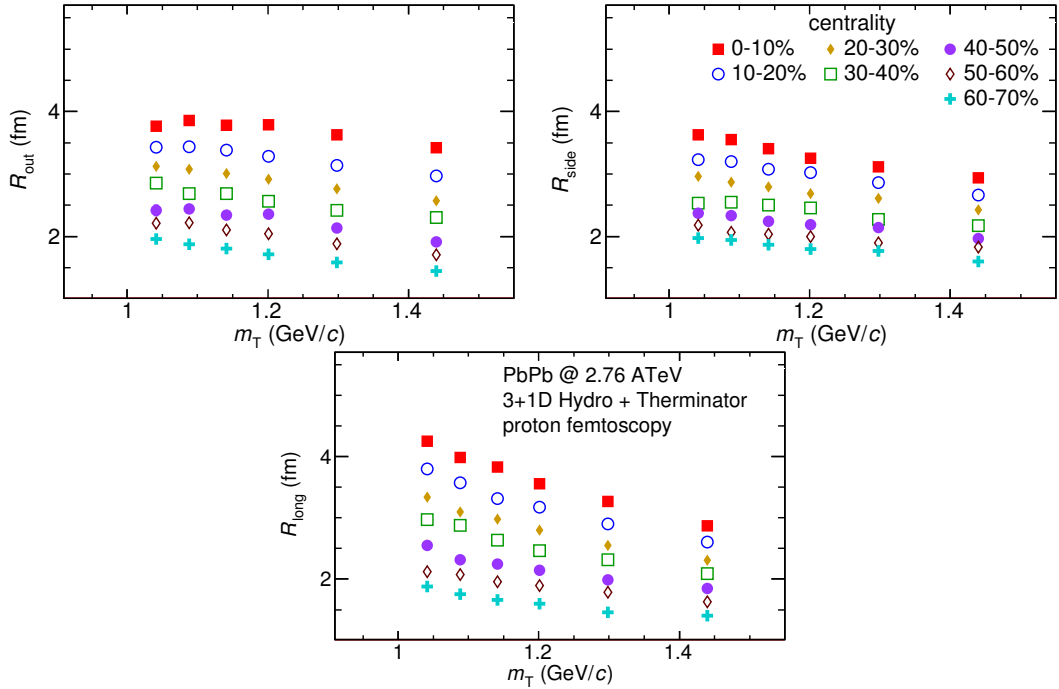


Figure 4.8: Femtoscopic radii extracted from two-proton correlation functions for different centrality bins as a function of  $m_T$ . [30].

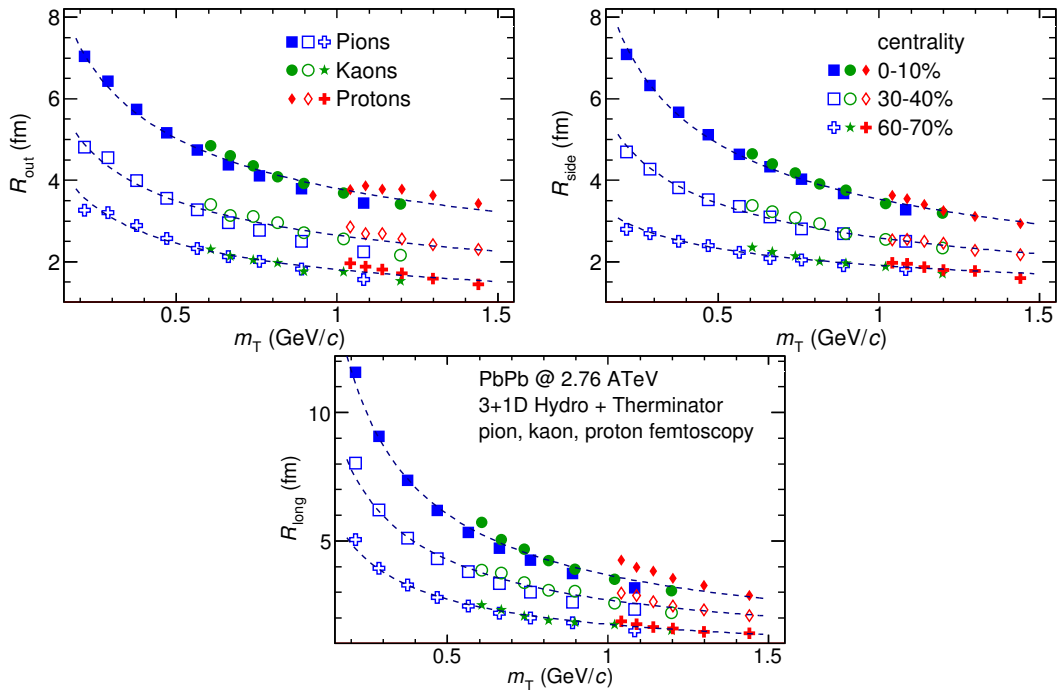


Figure 4.9: The results from the calculations for the pions, kaons and protons in for the three centralities presented on the common plot. One can notice that radii for particular centralities and different particle types follow the common power-law scaling. [30].

### 4.2.2 Scaling of one-dimensional radii

To the one-dimensional correlation function, the corresponding function in the PRF given by the Eq. 3.18 was fitted. The results from those fits are presented in the upper left plot in the Fig. 4.10. One immediately notices, that there is no common scaling of  $R_{inv}$  for different kind of particles. In the Fig. 4.9 the radii in the outward direction for the pions, kaons and protons for the same  $m_T$  are similar. However, when one performs a transition from the LCMS to the PRF, the  $R_{out}$  radius grows:

$$R_{out}^* = \gamma_T R_{out}, \quad (4.2)$$

where  $\gamma_T = m_T/m$ . For the lighter particles, the  $\gamma_T$  is much larger, hence the bigger growth of the  $R_{out}$  and the overall radius. This is visible in the Fig. 4.10 (top left), where the radii in the PRF for the lighter particles are bigger than for the heavier ones in case of the same  $m_T$  range.

In the Fig. 4.9 there is visible scaling in the outward, sideward and longitudinal direction. Hence one can expect an appearance of such scaling in a direction-averaged radius calculated in the LCMS. This radius is presented in the Fig. 4.10 (bottom) and indeed the  $R_{LCMS}$  exhibits power-law scaling with the  $m_T$ .

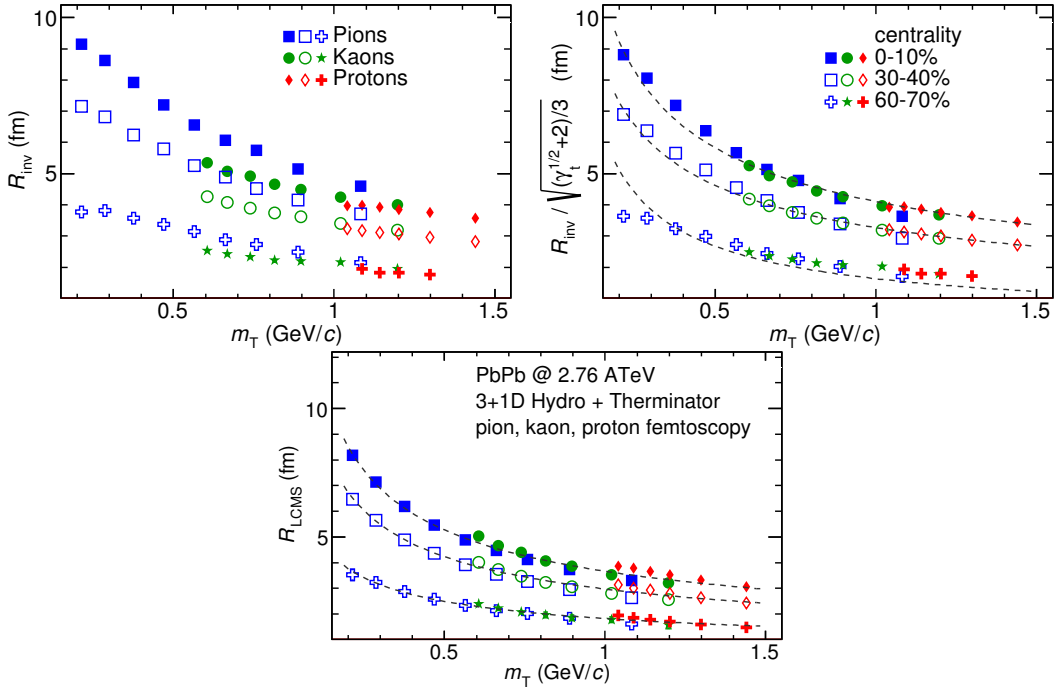


Figure 4.10: Top left: one-dimensional radius for pions, kaons and protons calculated in the PRF. Top right: the  $R_{inv}$  scaled by the proposed factor. Bottom: averaged one-dimensional radius in the LCMS for pions, kaons and protons. Only three centrality bins are shown for the better readability [30].

1005 One can try to account the effect of an increase of the radii in the outward  
 1006 direction by using the appropriate scaling factor. In the Fig. 4.10 (top right) there  
 1007 are femtoscopic radii in the LCMS divided by the proposed scaling factor:

$$f = \sqrt{(\sqrt{\gamma_T} + 2)/3} . \quad (4.3)$$

1008 The radii for pions, kaons and protons in the PRF after the division by  $f$  are  
 1009 following the power-law with the accuracy of 10%.

### 1010 4.3 Discussion of the results

1011 The femtoscopic radii obtained from the three-dimensional correlation func-  
 1012 tion fitting exhibit the  $m_T$  dependence described by the power law (Eq. 4.1). This  
 1013 scaling is preserved quite well with accuracy <10%. Observation of such scaling  
 1014 in a femtoscopic radii is a strong signal of appearance of a collective behaviour of  
 1015 a particle-emitting source created in the collision. The data used in the analysis  
 1016 was coming from the hydrodynamic model, hence one can indeed expect the  
 1017 appearance of this scaling. However, the results for pion femtoscopy from the  
 1018 ALICE at LHC are consistent with the data from analysis performed in this thesis  
 1019 (Fig. 4.6). This is a confirmation of an applicability of hydrodynamic models in a  
 1020 description of an evolution of a quark-gluon plasma.

1021 The  $\beta$  parameter calculated in the fitting of the power-law to the femtoscopic  
 1022 radii is in the order of 0.5 in case of the radii in the transverse plane. This value is  
 1023 consistent with the hydrodynamic predictions. In case of longitudinal radii, the  
 1024 exponent is bigger (greater than 0.7), which is an indication of a strong transversal  
 1025 expansion in the system [28].

1026 A scaling described above is visible in the LCMS, however due to limited stat-  
 1027 istics, analysis in this reference frame is not always possible. In such case one per-  
 1028 forms calculations in the PRF. The  $m_T$  scaling in the PRF is not observed - this has  
 1029 the trivial kinematic origin. A transition from the PRF to LCMS causes growth  
 1030 of the radius in the outward direction and the common power-law scaling for  
 1031 different particles breaks due to differences in the  $\gamma_T(m_T)$  for different particle  
 1032 types. However one can try to deal with the radius growth and restore the scal-  
 1033 ing by multiplying the radii  $R_{inv}$  by an approximate factor  $\sqrt{(\sqrt{\gamma_T} + 2)/3}$ . The  
 1034 scaled  $R_{inv}$  are following the power-law and could be used as a verification of  
 1035 hydrodynamic behaviour in the investigated particle source.

1036 The hadronic evolution and freeze-out in the THERMINATOR is followed  
 1037 by the resonance propagation and decay phase. A good accuracy of a scaling  
 1038 with the power-law indicated that the inclusion of the resonances does not  
 1039 break the  $m_T$  scaling. However, recent calculations including also hadron  
 1040 rescattering phase indicate that the scaling between pions and kaons is broken  
 1041 at the LHC [31].

# Conclusions

This thesis presents the results of the two-particle femtoscopy of different particle kinds produced in Pb-Pb collisions at the centre of mass energy  $\sqrt{s_{NN}} = 2.76$  TeV. The analysed data was generated by the THERMINATOR model using the (3+1)-dimensional hydrodynamic model.

The momentum correlations were studied for three different types of particle pairs: pions, kaons and protons. The data was analyzed for eight different sets of initial conditions corresponding the following centrality ranges: 0-5%, 0-10%, 10-20%, 20-30%, 30-40%, 40-50%, 50-60% and 60-70%. The correlation functions were calculated for the nine  $k_T$  bins from 0.1 GeV/c to 1.2 GeV/c. The calculations were performed using spherical harmonics decomposition of a three-dimensional correlation function. Using this approach, one can obtain full three-dimensional information about the source size using only the three coefficients:  $\Re C_0^0$ ,  $\Re C_2^0$  and  $\Re C_2^2$ . To perform further quantitative analysis, the femtoscopic radii were extracted through fitting.

The calculated correlation functions show expected increase of a correlation at low relative momenta in case of identical bosons (pions and kaons) and the decrease for the identical fermions (protons) respectively. This effect is especially visible in the first spherical harmonic coefficient  $\Re C_0^0$ . The other two components  $\Re C_2^0$  and  $\Re C_2^2$  are non-vanishing and are providing information about the ratios of radii in the outward, sideward and longitudinal directions.

An increase of width of a correlation function with the peripherality of a collision and the  $k_T$  is observed for pions, kaons and protons. This increase of femtoscopic radii (proportional to the inverse of width) with the  $k_T$  is related with the  $m_T$  scaling predicted by the hydrodynamic calculations.

Hydrodynamic equations are predicting appearance of femtoscopic radii common scaling for different kinds of particles with the  $m_T^{-0.5}$  in the LCMS. In the results in this work, a common scaling for different particle types is observed in the LCMS in the outward, sideward and longitudinal direction. The direction-averaged radius  $R_{LCMS}$  also shows this power-law behaviour. The fitting of a power law  $\alpha m_T^{-\beta}$  to the femtoscopic radii yielded the information, that the  $\beta$  exponent for the outward and sideward direction is in order of 0.5, which is consistent with the hydrodynamic predictions. For the longitudinal direction, the  $\beta$  is bigger ( $>0.7$ ) than in the other directions which is an indication of a strong transverse flow. Femtoscopic radii in LCMS are following the

1077 power-law scaling with the accuracy <5% for pions and kaons, and <10% in case  
1078 of protons.

1079 In case of the one-dimensional radii  $R_{inv}$  calculated in the PRF, no common  
1080 scaling is observed. This is a consequence of a transition from the LCMS to the  
1081 PRF, which causes the growth of radius in the outward direction and breaks the  
1082 scaling for different particles. However, one can try to correct the influence of  
1083 the  $R_{out}$  growth with an approximate factor  $\sqrt{(\sqrt{\gamma_T} + 2)/3}$ . After the division  
1084 of the  $R_{inv}$  by the proposed factor, the scaling is restored with an accuracy <10%.  
1085 In this way, the experimentally simpler measure of the one-dimensional radii can  
1086 be used as a probe for the hydrodynamic collectivity.

1087 The THERMINATOR model includes hydrodynamic expansion, statistical had-  
1088 ronization, resonance propagation and decay afterwards. The  $m_T$  scaling is pre-  
1089 dicted from the pure hydrodynamic calculations. However, this study shows,  
1090 that influence of the resonances on this scaling is less than 10%.

1091 **Appendix A**

1092 **Scripts for events generation**

1093 In order to perform analysis with sufficient statistics, a large amount of gen-  
1094 erated events was required. To handle this task of generation large amount of  
1095 data, a computer cluster at Faculty of Physics at Warsaw University of Techno-  
1096 logy was used. This cluster consists of 20 nodes with the following hardware  
1097 configuration: Intel® Core™ 2 Quad CPU Q6600 @ 2.40GHz, 8GB RAM with Sci-  
1098 entific Linux 5.8. The communication between nodes is realized by the TORQUE  
1099 Resource Manager [32]. To control process of launching multiple event generat-  
1100 ors and collecting the data, the following scripts were written using Bash script-  
1101 ing language:

1102 **skynet.sh** This is a script in a form of a batch job for TORQUE. It simply  
1103 launches multiple THERMINATOR processes in the same working directory  
1104 with the separate output directory for each job. This solution has two  
1105 advantages: saves space and computation time. A single freeze-out  
1106 hypersurface file has size about 230 MB and when running 20 instances  
1107 of generator this approach allows to avoid time- and space-consuming  
1108 copying of the whole THERMINATOR directory before running the  
1109 application. The second advantage is a sharing of files containing  
1110 information about particles' multiplicities and maximum integrands  
1111 between generator processes (more detailed description is in Section 2.3).  
1112 One can simply execute this batch job using the following command (an  
1113 example usage):

1114 qsub -q long -t 0-19 skynet.sh -v dir=th\_5.7,events=6000  
1115 It adds 20 event generators (with task ids from 0 to 19) to the queue, sets  
1116 the THERMINATOR directory as th\_5.7 and sets a number of simulated  
1117 events to 6000 for each process. One has to execute this command in the  
1118 directory one level higher than th\_5.7 directory.

1119 **merge\_events.sh** After the generation process, one has to merge calculated  
1120 events into one directory. This task requires renaming of a large number of  
1121 THERMINATOR event files. Each event generator job produces files named

1122 with a certain pattern, starting from event000.root with increasing number.  
1123 In order to move the event files and preserve continuity in the numbering,  
1124 a simple script was written. An example of usage:  
1125 `find /data/source -iname "event*.root" -type f \`  
1126 `| merge_events.sh`  
1127 This command will find all the event files in the directory /data/source,  
1128 move and rename those files accordingly to the enumeration of events in  
1129 the current working directory.

1130 Sources of these two scripts are available on-line at <https://github.com/carbolymer/msc/tree/master/alix>.

<sub>1132</sub> **Appendix B**

<sub>1133</sub> **Macros for fitting**

1134 Appendix C

1135 Plotting scripts

<sup>1136</sup>

# Bibliography

- <sup>1137</sup> [1] Standard Model of Elementary Paticles - Wikipedia, the free encyclopedia  
<sup>1138</sup> [http://en.wikipedia.org/wiki/standard\\_model](http://en.wikipedia.org/wiki/standard_model).
- <sup>1139</sup> [2] R. Aaij et al. (LHCb Collaboration). Observation of the resonant character of  
<sup>1140</sup> the  $z(4430)^-$  state. *Phys. Rev. Lett.*, 112:222002, Jun 2014.
- <sup>1141</sup> [3] Donald H. Perkins. *Introduction to High Energy Physics*. Cambridge University Press,  
<sup>1142</sup> fourth edition, 2000. Cambridge Books Online.
- <sup>1143</sup> [4] G. Odyniec. *Phase Diagram of Quantum Chromo-Dynamics* - course at Faculty  
<sup>1144</sup> of Physics, Warsaw University of Technology, Jun 2012.
- <sup>1145</sup> [5] J. Beringer et al. (Particle Data Group). The Review of Particle Physics. *Phys.  
Rev.*, D86:010001, 2012.
- <sup>1147</sup> [6] Z. Fodor and S.D. Katz. The Phase diagram of quantum chromodynamics.  
<sup>1148</sup> 2009.
- <sup>1149</sup> [7] F. Karsch. Lattice results on QCD thermodynamics. *Nuclear Physics A*, 698(1-  
<sup>1150</sup> 4):199 – 208, 2002.
- <sup>1151</sup> [8] Adam Kisiel. *Studies of non-identical meson-meson correlations at low relative ve-  
locities in relativistic heavy-ion collisions registered in the STAR experiment*. PhD  
<sup>1152</sup> thesis, Warsaw University of Technology, Aug 2004.
- <sup>1153</sup> [9] J. Bartke. *Relativistic Heavy Ion Physics*. World Scientific Pub., 2009.
- <sup>1155</sup> [10] W. Florkowski. *Phenomenology of Ultra-Relativistic Heavy-Ion Collisions*.  
<sup>1156</sup> World Scientific, 2010.
- <sup>1157</sup> [11] Science Grid This Week, October 25, 2006 - Prob-  
<sup>1158</sup> ing the Perfect Liquid with the STAR Grid  
<sup>1159</sup> [http://www.interactions.org/sgtw/2006/1025/star\\_grid\\_more.html](http://www.interactions.org/sgtw/2006/1025/star_grid_more.html).
- <sup>1160</sup> [12] K. Grebieszkow. Fizyka zderzeń ciężkich jonów,  
<sup>1161</sup> <http://www.if.pw.edu.pl/~kperl/hip/hip.html>.
- <sup>1162</sup> [13] Ulrich W. Heinz. From SPS to RHIC: Maurice and the CERN heavy-ion  
<sup>1163</sup> programme. *Phys.Scripta*, 78:028005, 2008.

- 1164 [14] J. Adams et al. Identified particle distributions in pp and Au+Au collisions  
1165 at  $s(\text{NN})^{**}(1/2) = 200 \text{ GeV}$ . *Phys.Rev.Lett.*, 92:112301, 2004.
- 1166 [15] G. David, R. Rapp, and Z. Xu. Electromagnetic Probes at RHIC-II. *Phys.Rept.*,  
1167 462:176–217, 2008.
- 1168 [16] A. Marin et al. Dilepton measurements with CERES. *PoS*, CPOD07:034,  
1169 2007.
- 1170 [17] J. Adams et al. Experimental and theoretical challenges in the search for the  
1171 quark gluon plasma: The STAR Collaboration’s critical assessment of the  
1172 evidence from RHIC collisions. *Nucl.Phys.*, A757:102–183, 2005.
- 1173 [18] Adam Kisiel, Tomasz Taluc, Wojciech Broniowski, and Wojciech  
1174 Florkowski. THERMINATOR: THERMal heavy-IoN generATOR. *Comput.Phys.Commun.*, 174:669–687, 2006.
- 1176 [19] Mikolaj Chojnacki, Adam Kisiel, Wojciech Florkowski, and Wojciech Bro-  
1177 niowski. THERMINATOR 2: THERMal heavy IoN generATOR 2. *Comput.Phys.Commun.*, 183:746–773, 2012.
- 1179 [20] I. et al (BRAHMS Collaboration) Bearden. Charged meson rapidity distri-  
1180 butions in central Au + Au collisions at  $\sqrt{s_{\text{NN}}} = 200 \text{ GeV}$ . *Phys. Rev. Lett.*,  
1181 94:162301, Apr 2005.
- 1182 [21] W. Israel and J.M. Stewart. Transient relativistic thermodynamics and kin-  
1183 etic theory. *Annals of Physics*, 118(2):341 – 372, 1979.
- 1184 [22] Piotr Bożek. Flow and interferometry in (3 + 1)-dimensional viscous hydro-  
1185 dynamics. *Phys. Rev. C*, 85:034901, Mar 2012.
- 1186 [23] K. Kovtun, P. D. T. Son, and A. O. Starinets. Viscosity in strongly interacting  
1187 quantum field theories from black hole physics. *Phys. Rev. Lett.*, 94:111601,  
1188 Mar 2005.
- 1189 [24] Fred Cooper and Graham Frye. Single-particle distribution in the hydro-  
1190 dynamic and statistical thermodynamic models of multiparticle production.  
1191 *Phys. Rev. D*, 10:186–189, Jul 1974.
- 1192 [25] Adam Kisiel. Nonidentical-particle femtoscopy at  $\sqrt{s_{\text{NN}}} = 200 \text{ GeV}$  in hy-  
1193 drodynamics with statistical hadronization. *Phys. Rev. C*, 81:064906, Jun  
1194 2010.
- 1195 [26] Adam Kisiel and David A. Brown. Efficient and robust calculation of femto-  
1196 scopic correlation functions in spherical harmonics directly from the raw  
1197 pairs measured in heavy-ion collisions. *Phys.Rev.*, C80:064911, 2009.
- 1198 [27] S. Pratt. Pion Interferometry for Exploding Sources. *Phys.Rev.Lett.*, 53:1219–  
1199 1221, 1984.

- 1200 [28] S.V. Akkelin and Yu.M. Sinyukov. The HBT-interferometry of expanding  
1201 inhomogeneous sources. *Z.Phys.*, C72:501–507, 1996.
- 1202 [29] K. Aamodt et al. Two-pion Bose-Einstein correlations in central Pb-Pb colli-  
1203 sions at  $\sqrt{s_{NN}} = 2.76$  TeV. *Phys.Lett.*, B696:328–337, 2011.
- 1204 [30] A. Kisiel, M. Galazyn, and P. Bozek. Pion, kaon, and proton femtoscopy in  
1205 Pb–Pb collisions at  $\sqrt{s_{NN}}=2.76$  TeV modeled in 3+1D hydrodynamics. 2014.
- 1206 [31] V.M. Shapoval, P. Braun-Munzinger, Iu.A. Karpenko, and Yu.M. Sinyukov.  
1207 Femtoscopy correlations of kaons in  $Pb + Pb$  collisions at LHC within hy-  
1208 drokinetic model. 2014.
- 1209 [32] TORQUE Resource Manager - An open source resource manager  
1210 providing control over batch jobs and distributed compute nodes  
1211 <http://www.adaptivecomputing.com/products/open-source/torque/>.

# List of Figures

1.1	The Standard Model of elementary particles [1]. . . . .	3
1.2	A string breaking and a creation of a new quark-anti-quark pair [4]. . . . .	5
1.3	The coupling parameter $\alpha_s$ dependence on four-momentum transfer $Q^2$ [5]. . . . .	6
1.4	The QCD potential for a quark-antiquark pair as a function of distance for different temperatures. A value of a potential decreases with the temperature [4]. . . . .	7
1.5	A number of degrees of freedom as a function of a temperature [7]. . . . .	7
1.6	Phase diagram coming from the Lattice QCD calculations [8]. . . . .	8
1.7	Left: stages of a heavy ion collision simulated in the UrQMD model. Right: schematic view of a heavy ion collision evolution [8]. . . . .	9
1.8	Overlapping region which is created in heavy ion collisions has an almond shape. Visible x-z plane is a <i>reaction plane</i> . The x-y plane is a <i>transverse plane</i> . The z is a direction of the beam [11]. . . . .	11
1.9	Cross-section of a heavy ion collision in a transverse plane. The $b$ parameter is an <i>impact parameter</i> - a distance between centers of nuclei during a collision. An impact parameter is related with the centrality of a collision and a volume of the quark-gluon plasma [12]. . . . .	12
1.10	<i>Lower:</i> The elliptic flow $v_2$ follows the hydrodynamical predictions for an ideal fluid perfectly. Note that > 99% of all final hadrons have $p_T < 1.5 \text{ GeV}/c$ . <i>Upper left:</i> The $v_2$ plotted versus transverse kinetic energy $KE_T = m_T - m_0 = \sqrt{p_T^2 + m_0^2} - m_0$ . The $v_2$ follows different universal curves for mesons and baryons. <i>Upper right:</i> When scaled by the number of valence quarks, the $v_2$ follows the same universal curve for all hadrons and for all values of scaled transverse kinetic energy [13]. . . . .	13
1.11	Invariant yield of particles versus transverse mass $m_T = \sqrt{p_T^2 + m_0^2}$ for $\pi^\pm$ , $K^\pm$ , $p$ and $\bar{p}$ at mid-rapidity for p+p collisions (bottom) and Au+Au events from 70-80% (second bottom) to 0-5% (top) centrality [14]. . . . .	14

1243	1.12 Thermal photons spectra for the central Au+Au collisions at	
1244	$\sqrt{s_{NN}} = 200$ GeV computed within different hydrodynamical	
1245	models compared with the pQCD calculations (solid line) and	
1246	experimental data from PHENIX (black dots) [15]. . . . .	15
1247	1.13 Left: Invariant mass spectrum of $e^+e^-$ pairs in Pb+Au collisions	
1248	at 158A GeV compared to the sum coming from the hadron decays	
1249	predictions. Right: The expectations coming from model calcula-	
1250	tions assuming a dropping of the $\rho$ mass (blue) or a spread of the	
1251	$\rho$ width in the medium (red) [16]. . . . .	16
1252	1.14 Azimuthal angle difference $\Delta\phi$ distributions for different colliding	
1253	systems at $\sqrt{s_{NN}} = 200$ GeV. Transverse momentum cut: $p_T > 2$	
1254	GeV. For the Au+Au collisions the away-side jet is missing [17]. . .	17
1255	2.1 The cascade decay in the single freeze-out model. An unstable res-	
1256	onance $x_N$ is formed at the freeze-out hypersurface and travels for	
1257	the time $\tau_N$ depending on its lifetime and decays. If the products	
1258	are also resonances ( $x_{N-1}, x_2$ ) they decay further until the stable	
1259	particles are formed ( $x_1$ ) [18]. . . . .	24
1260	3.1 Bertsch-Pratt direction naming convention used in heavy ion col-	
1261	lision. . . . .	26
1262	3.2 The pair wave function is a superposition of all possible states. In	
1263	case of particle interferometry it includes two cases: particles with	
1264	momenta $p_1, p_2$ registered by detectors $A, B$ and $p_1, p_2$ registered	
1265	by $B, A$ respectively. . . . .	27
1266	3.3 An averaged three-dimensional Gaussian source function with dif-	
1267	ferent widths was averaged into one-dimensional function. To il-	
1268	lustrate deformations, one-dimensional Gaussian distribution was	
1269	fitted. . . . .	30
1270	3.4 Correlation function width dependence on total pair momentum.	
1271	Pion pairs with a large total momentum have a wider correlation	
1272	(smaller apparent source) [27]. . . . .	34
1273	4.1 Spherical harmonics coefficients of the two-pion correlation func-	
1274	tion. From the top left: $\Re C_0^0$ , $\Re C_2^0$ and $\Re C_2^2$ . Only few centrality	
1275	bins are presented for increased readability. . . . .	37
1276	4.2 Spherical harmonics coefficients of the two-kaon correlation func-	
1277	tion. From the top left: $\Re C_0^0$ , $\Re C_2^0$ and $\Re C_2^2$ . Only few centrality	
1278	bins are presented for increased readability. The $\Re C_2^2$ is noisy, but	
1279	one can still notice that it differs from zero and is becoming negative. 38	

1280	4.3	Spherical harmonics coefficients of the two-proton correlation function. From the top left: $\Re C_0^0$ , $\Re C_2^0$ and $\Re C_2^2$ . Only few centrality bins are presented for increased readability. The $\Re C_2^0$ and $\Re C_2^2$ are noisy, but one can still notice, that they differ from zero and are becoming positive. . . . .	39
1281			
1282			
1283			
1284			
1285	4.4	One-dimensional correlation function for pions (top left), kaons (top right) and protons (bottom) for different centralities. . . . .	40
1286			
1287	4.5	One-dimensional correlation functions for pions, kaons and protons, for the same centrality bin and different $k_T$ ranges. The plot was zoomed in to the region which illustrates the $k_T$ dependence in the best way. Only few of the calculated ranges are presented for better readability. . . . .	41
1288			
1289			
1290			
1291			
1292	4.6	Femtoscopic radii in LCMS coming from two-pion correlation functions for all centrality bins as a function of $m_T$ . The dashed lines are power-law fits. The most central collisions (0-5%) are compared to the results from ALICE [29]. The two datasets are shifted to the right for visibility [30]. . . . .	42
1293			
1294			
1295			
1296			
1297	4.7	Femtoscopic radii extracted from two-kaon correlation functions for different centrality bins as a function of $m_T$ . [30]. . . . .	43
1298			
1299	4.8	Femtoscopic radii extracted from two-proton correlation functions for different centrality bins as a function of $m_T$ . [30]. . . . .	44
1300			
1301	4.9	The results from the calculations for the pions, kaons and protons in for the three centralities presented on the common plot. One can notice that radii for particular centralities and different particle types follow the common power-law scaling. [30]. . . . .	45
1302			
1303			
1304			
1305	4.10	Top left: one-dimensional radius for pions, kaons and protons calculated in the PRF. Top right: the $R_{inv}$ scaled by the proposed factor. Bottom: averaged one-dimensional radius in the LCMS for pions, kaons and protons. Only three centrality bins are shown for the better readability [30]. . . . .	46
1306			
1307			
1308			
1309			